Upper-mantle anisotropy in the southeastern margin of Tibetan Plateau revealed by fullwave SKS splitting intensity tomography

Yi Lin[1,2], Li Zhao[1,3]

[1] School of Earth and Space Sciences, Peking University, Beijing 100871, China.

[2] Key Laboratory of Earth Exploration and Information Techniques of the China Ministry of Education, Chengdu University of Technology, Chengdu 610059, China.

[3] Hebei Hongshan National Geophysical Observatory, Peking University, Beijing 100871, China.

Corresponding author: L. Zhao (lizhaopku@pku.edu.cn)

Key Points:

- A 3D shear-wave anisotropy model for the SE margin of the Tibetan Plateau is obtained by fullwave SKS splitting intensity tomography
- Result shows a decoupling of lithosphere and asthenosphere deformations in the region, but a coupling under Tibetan Plateau
- Lithospheric anisotropy has a complex pattern, whereas asthenospheric anisotropy follows the APM

Abstract

The southeastern margin of the Tibetan Plateau has undergone complex deformation since the Cenozoic, resulting in a high level of seismicity and seismic hazard. Knowledge about the seismic anisotropy provides important insight about the deformation mechanism and the regional seismotectonics beneath this tectonically active region. In this study, we conduct fullwave multi-scale tomography to investigate the seismic anisotropy in the southeastern margin of the Tibetan Plateau. Broadband records at 111 permanent stations in the region from 470 teleseismic events are used to obtain 5,216 high-quality SKS splitting intensity measurements, which are then inverted in conjunction with 3D sensitivity kernels to obtain an anisotropic model with multi-scale resolution. Resolution tests show that our dataset recovers anisotropy anomalies reasonably well on the scale of 1º x 1º horizontally and ~100 km vertically. Our result suggests that in the southeastern margin of the Tibetan Plateau the deformation in the lithosphere and asthenosphere are decoupled. The anisotropy in the lithosphere varies both laterally and vertically as a result of dynamic interactions of neighboring blocks as well as lithospheric reactivation. The anisotropy in the asthenosphere largely follows the direction of regional absolute plate motion. The SKS splittings observed at the surface are shown to be consistent with the vertical integral of our depth-dependent anisotropy model over lithospheric and asthenospheric depths.

Keywords: seismic anisotropy; splitting intensity; finite-frequency; fullwave tomography; southeastern Tibetan Plateau

Plain Language Summary

The southeastern margin of the Tibetan Plateau has undergone significant deformation since the Cenozoic due to the collision between the Eurasian and Indian plates in the south and interactions with the Yangtze Craton in the east. Knowledge about the upper mantle seismic anisotropy helps us understand the

deformation and dynamic evolution. In this study, we conduct fullwave multi-scale anisotropy tomography for the southeastern margin of the Tibetan Plateau using 5,216 high-quality SKS splitting intensity measurements obtained from the broadband records of 470 teleseismic events at 111 stations. Our result shows a decoupling between the lithosphere and asthenosphere deformations in the southeastern margin of the Tibetan Plateau. The anisotropy in the lithosphere varies both laterally and vertically as a result of the dynamic interactions of neighboring blocks as well as lithospheric reactivation. The anisotropy in the asthenosphere is largely parallel to the regional absolute plate motion, and the SKS splitting observed at the surface is the result of vertical integration of the anisotropy effect through the lithosphere and asthenosphere.

1 Introduction

The ongoing Indian-Eurasian continental collision has resulted in the largest plateau on Earth and caused widespread deformation in central and east Asia (Yin & Harrison, 2000; Kind et al., 2002). Despite numerous efforts, questions remain about the dynamics of the lithospheric deformation and asthenosphere flow beneath the Tibetan Plateau and the surrounding regions (Royden et al., 2008).

The southeastern (SE) margin of the Tibetan Plateau involves many active tectonic blocks (Figure 1), including the Songpan-Ganzi Terrane (SGT), the Sichuan Basin (SCB), the Sichuan-Yunnan Rhombic Block (SYRB), the Indo-China Block (ICB), the Qiangtang Block (QTB), and the Yangtze Craton (YTC). The SGT is part of central Tibetan Plateau. Its eastern part is separated from the SCB and SYRB by the Longmenshan Fault (LMSF) and Lijiang-Xiaojinhe Fault (LJ-XJHF), respectively, and bounded in the south by the Jinshajiang Fault (JSJF) from the QTB. The convergence between the Indian and Eurasian plates caused the SGT to expand eastward against the SCB during the Cenozoic (Yin & Harrison, 2000). GPS observations show eastward crustal motion of the eastern SGT with the crustal strain rate decreasing abruptly from ~20 mm/year (relative to the YTC reference frame) in the interior SGT to ~3–4 mm/year or less in the vicinity of central and southern segments of the LMSF, indicating that the eastward expansion of the SGT is apparently resisted by the SCB (Shen et al., 2005; Zhang, 2013) In addition, there is also an apparent clockwise rotation of the GPS velocities around the Eastern Himalaya Syntax (EHS). Low-velocity and high-conductivity anomalies in the mid-lower crust under the SGT revealed by geophysical studies (Zhao et al., 2012; Bao et al., 2020) suggest the existence of mid-lower crustal flow. However, these geophysical anomalies show strong lateral heterogeneity in eastern Tibet, implying a complex process of deformation in the region. The SCB and SYRB are both parts of the YTC (Zhang et al., 2013; Li et al., 2021). The former forms the rigid and stable northwestern margin of the YTC, while the crust of the latter is extruding southeastward along the Anninghe-Zemuhe Fault (ANH-ZMHF) and Xiaojiang Fault

(XJF) in the east and the Red River Fault (RRF) in the southwest (Zhang et al., 2003). The Lancangjiang Fault (LCJF) separates the narrow QTB in the east and the ICB in the west. Crustal movements are predominantly characterized by a clockwise rotation around the Eastern Himalayan Syntaxis (EHS), transforming the movement of the plateau material from eastward north of the syntaxis to southeastward and southward further south (Wang & Shen, 2020).

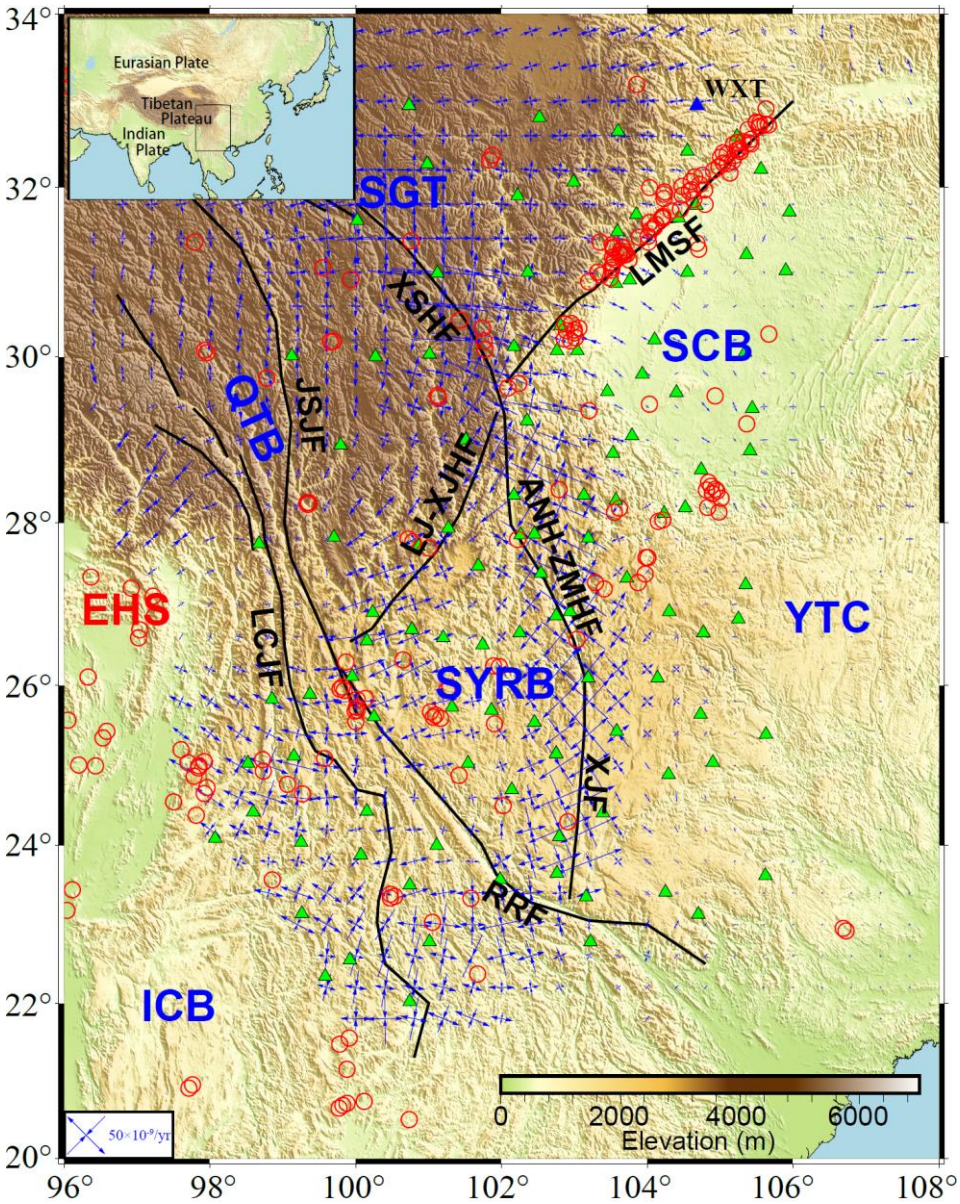

Figure 1. Map of the tectonic environment of SE margin of Tibetan Plateau with seismic stations (green-filled triangles) and epicenters (red open circles) of earthquakes of magnitude 5 and above from 2000 to

2022. The blue triangle marks the station WXT for which SKS waveforms, splitting intensities and sensitivity kernels are shown in Figures 4, 5 and 7, respectively. Major active faults are shown by thick black lines with abbreviated names in black, including LMSF: Longmenshan Fault; XSHF: Xianshuihe Fault; JSJF: Jinshajiang Fault; LCJF: Lancangjiang Fault; LJ-XJHF: Lijiang-Xiaojinhe Fault; ANH-ZMHF: Anninghe-Zemuhe Fault; XJF: Xiaojiang Fault; and RRF: Red River Fault. Major active tectonic blocks are indicated by abbreviated texts in blue, including SGT: Songpan-Ganzi Terrane; SCB: Sichuan Basin; QTB: Qiangtang Block; SYRB: Sichuan-Yunnan Rhombic Block; YTC: Yangtze Craton; and ICB: Indo-China Block. EHS stands for the Eastern Himalaya Syntax. Blue cross arrows show the surface strain rate derived from GPS observation (Wang & Shen, 2020). Background color shows the topography. The black box in the inset map indicates the location of the main figure.

Over the past two decades, a large number of seismic stations have been deployed in the SE margin of the Tibetan Plateau. Waveforms recorded by the growing number of broadband stations have provided crucial data for studying the structure and dynamics of the crust and upper mantle beneath the region, such as variation in crustal thickness (Wang et al., 2017; Xu et al., 2020), widespread low-velocity anomalies in mid-lower crust revealed by receiver function analysis (Hu et al., 2005; Xu et al., 2007; Zhang et al., 2009; Wang et al., 2010), Lg-wave high-attenuation zones (Zhao et al., 2013; Wei & Zhao, 2019), joint inversion of receiver function and surface wave dispersion (Liu et al., 2014), and body- and surface-wave tomographies (Huang et al., 2002; Wang et al., 2003; Huang et al., 2009; Li et al., 2009; Yang et al., 2019; Wei & Zhao, 2022).

Across the LMSF, the drastic change in elevation from ~5–6 km in the west to a few hundred meters in the east suggests significant variations in the lithospheric thickness, as illustrated in Figure 2, where the global model LITHO1.0 (Pasyanos et al., 2014) is shown north of 27ºN. South of 27ºN, LITHO1.0 is rather uniform, and the regional model of Yang et al. (2017) is depicted. In this region, the lithosphere has a thickness of less than 100 km in the northern and southern parts but ~150 km at the mid latitudes. The thickest lithosphere is more than 200 km beneath the SCB.

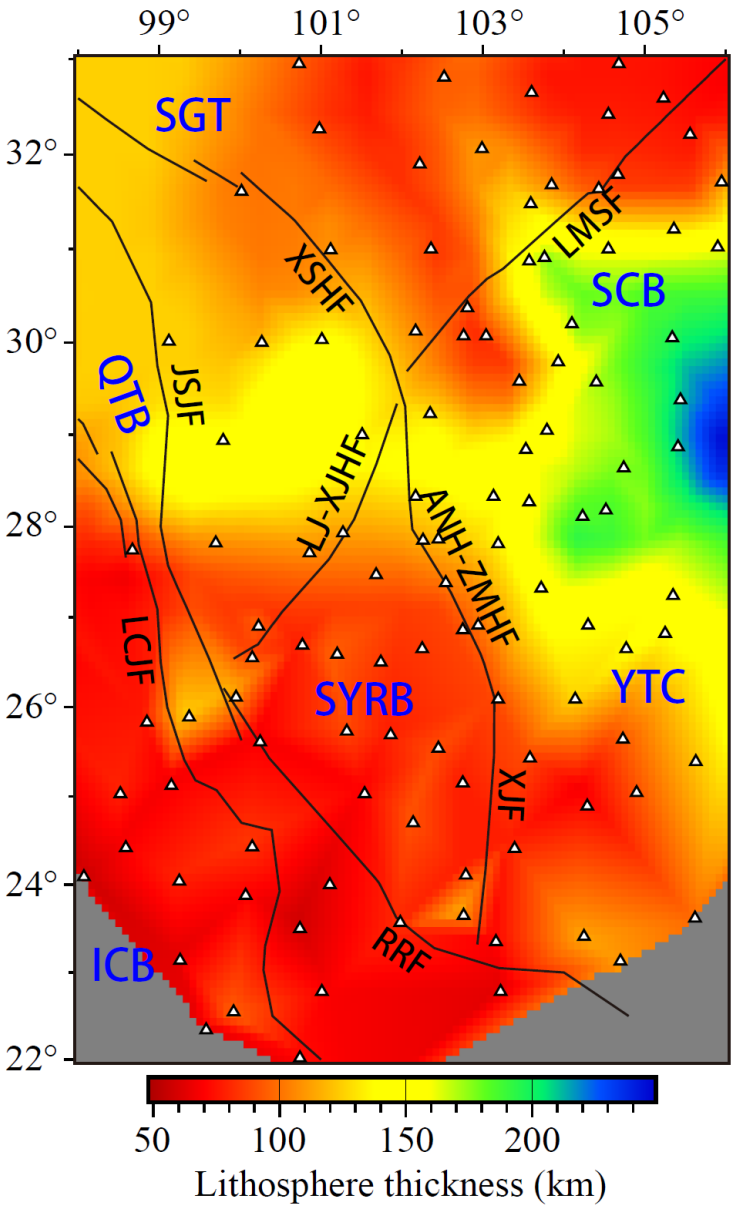

Figure 2. Lithosphere thickness map. The global model LITHO1.0 (Pasyanos et al., 2014) is shown for the region north of 27ºN, whereas to the south the regional model of Yang et al. (2017) is depicted. Names of major faults and tectonic blocks are the same as in Figure 1.

Seismic anisotropy in the upper mantle is an important proxy for deformation. There have been numerous studies devoted to crustal anisotropy beneath the SE Tibetan Plateau utilizing different methods, such as Pms splitting (Sun et al., 2012; Cai et al., 2016; Han et al., 2020), anisotropic tomography of P and Pn waves (Lei et al., 2014; Huang et al., 2018), surface wave anisotropic tomography (Yang et al.,

2010; Yao et al., 2010; Legendre et al., 2015; Zhang et al., 2023), and the splitting of shear waves (Shi et al., 2012). In the upper crust, the fast axis directions are mainly parallel to the strike of active faults (e.g., Yao et al., 2010; Shi et al., 2012; Huang et al., 2018), whereas the anisotropic pattern in the lower crust is different. Huang et al. (2018) showed that the fast velocity direction deviates from the strikes of active faults significantly using P-wave anisotropic tomography. Han et al. (2020) used Markov-chain Monte Carlo inversion of receiver functions to isolate the effect of potential dipping interfaces. Their results showed that the fast axis directions in the lower crust are in good agreement with topography, implying that the gravitational potential may be the driving force for the crustal deformation in southeastern Tibet.

XKS-wave splitting is routinely used to investigate the anisotropic structure in the upper mantle (Long & Becker, 2010). Flesch et al. (2005) jointly analyzed GPS, surface geology and shear-wave splitting measurements and argued for vertically coherent deformation in the crust and upper mantle in the Tibetan Plateau but a decoupling in Yunnan Province in southwestern China. Lev et al. (2006) also suggested a lithosphere-asthenosphere decoupling in Yunnan using shear-wave splitting observations, but they were not able to determine the degree of coupling beneath the Tibetan Plateau. Based on a joint analysis of a larger dataset of shear-wave splitting measurements and GPS observations, Wang et al. (2008) argued for crust-mantle coupling in the Tibetan Plateau and the surrounding regions.

Substantial efforts have been made to develop a theoretical framework as well as practical strategies for inversion for the 3D distribution of anisotropy. A fullwave approach has been developed for the measurement of shear-wave splitting intensities and interpretation in terms of shear-wave azimuthal anisotropy parameters (Chevrot, 2000; Favier & Chevrot, 2003; Chevrot, 2006; Sieminski et al., 2008; Monteiller & Chevrot, 2011; Lin et al., 2014a), which has been applied to anisotropy tomographies for southern California (Monteiller & Chevrot, 2011; Lin et al., 2014b), the High Lava Plain (Mondal & Long, 2020), and the southeastern Tibetan Plateau (Huang & Chevrot, 2021). The depth variations of anisotropy obtained

by these studies have shed new lights in understanding the sources of anisotropy and the associated mantle dynamics.

In this study, we conduct a fullwave multiscale anisotropy tomography for the SE margin of Tibetan Plateau. We collect seismic records at regional permanent broadband stations from globally distributed earthquakes and obtain high-quality measurements of SKS splitting intensities. We then invert the splitting intensities using a wavelet-based parameterization of the 3D model to achieve a multi-scale resolution of the anisotropic structure. We also provide an interpretation of our anisotropic model for the SE margin of Tibetan Plateau in terms of regional geodynamics.

2 Data and Methods

2.1 Waveform records

We collect waveforms recorded by 111 permanent broadband stations (green triangles in Figure 1) deployed in the study region. To guarantee a wide range of azimuthal distribution, we select events of magnitude $Mw \geq 5.5$ from 2009 to 2020, located in the epicentral distance range of 90°–130°. After quality control of the waveforms and removal of outliers of the data (see Section 2.2), a total of 470 events are used in the subsequent inversions. Figure 3 displays the event distribution.

2.2 Splitting intensity measurements

Shear-wave splitting measurement is nowadays a routine procedure in the study of seismic anisotropy. Several previous studies have documented the measured SKS splitting parameters (fast directions and delay times) at stations in our study region (e.g., Chang et al., 2015; Yang et al., 2018; Liu et al., 2020; Huang & Chevrot, 2021; Li et al., 2021). In this study, we invert for the 3D anisotropy structure using the splitting intensity (SI) measurements obtained by computing the zero-lag cross-correlation between the transverse-component record and the time derivative of the radial-component record (Chevrot, 2000).

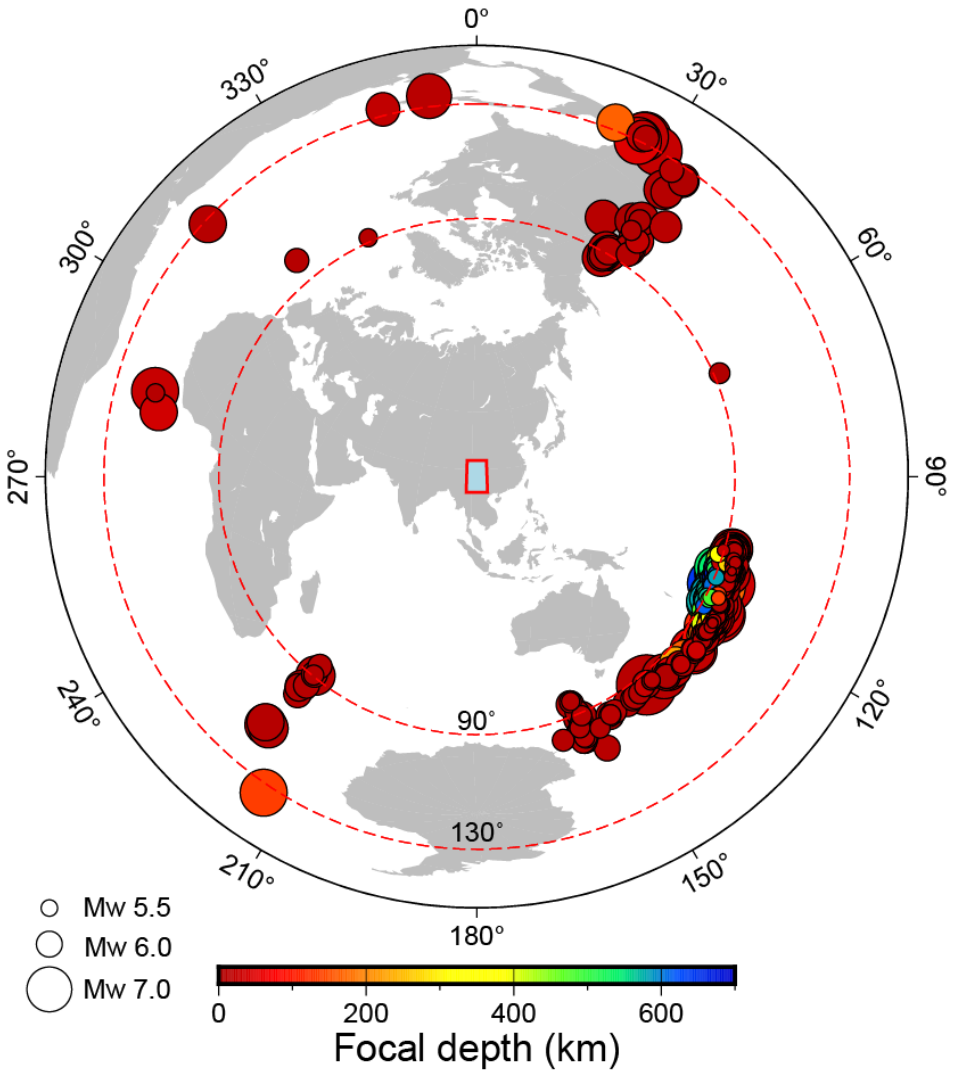

Figure 3. Distribution of 470 teleseismic events used for SKS splitting intensity inversion in this study. Events of magnitudes Mw5.5 and greater in the epicentral distance range of 90°–130° during 2009–2020 are selected. The red box in the center indicates the study area.

For a given station, the SI of the SKS wave from the *i*-th event is defined as

$$S_i = -2\frac{\int_{t_{i1}}^{t_{i2}} \dot{u}_i^R(t) u_i^T(t) dt}{\int_{t_{i1}}^{t_{i2}} [\dot{u}_i^R(t)]^2 dt}, \quad (1)$$

where $[t_{i1}, t_{i2}]$ is the time window for the SKS wave, and $u_i^R(t)$ and $u_i^T(t)$ are the radial and transverse-component records, respectively, from the *i*-th event. A dot above a variable indicates derivative with respect to time. The conventional SKS splitting parameters at the given station, namely the fast-direction

azimuth θ and delay time Δt, are related to the SIs measured at the station from all events through a sinusoidal curve fitting (Chevrot, 2000; Lin et al., 2014a):

$$S_i = \Delta t \sin 2(\theta - \theta_i^b), \tag{2}$$

where θ_i^b is the back azimuth of the *i*-th event.

In this study, we obtain the SI measurements of SKS waves with the help of SplitRacer (Link et al., 2022), an efficient and automatic toolbox developed for the measurement and quality control of XKS splittings. An example of SplitRacer processing is shown in Figure 4. We use SplitRacer to determine the SKS time window automatically, followed by a manual check on the quality of the SKS signals. Then, we calculate the SIs using Eq. (1). The period band we use in this study is 8–50 s considering the dominant periods of the SKS signals as well as minimizing the interference with neighboring phases. As shown in Figure 4, the spectral powers of the radial- and transverse-component records are calculated by the short-time Fourier transform (Quatieri, 2006) and summed. Then, the dominant frequency band of the SKS waveform can be identified (between the red dashed horizontal lines in Figure 4c). At each time, the powers within the dominant frequency band are summed (Figure 4d), which defines the SKS window by the two crossing points at 50% of the peak level (vertical green lines in Figure 4d). The final SKS window is given by either expanding or shrinking the 50% energy window to a fixed 30-s window (red vertical lines). After completing the quality check using SplitRacer, we obtain a total of 12,457 SKS wave SI measurements.

Following Chevrot (2000), we estimate the uncertainty of each SI measurement using the following equation

$$\sigma_i = \sqrt{\frac{1}{N_i}\left\{\sum_{j=1}^{N_i}\left[u_i^T(t_j)\right]^2 - \frac{S_i^2}{4}\sum_{j=1}^{N_i}\left[\dot{u}_i^R(t_j)\right]^2\right\}}, \tag{3}$$

where S_i is the *i*-th SI measurement, and N_i is the number of time samples used for the window to obtain the measurement.

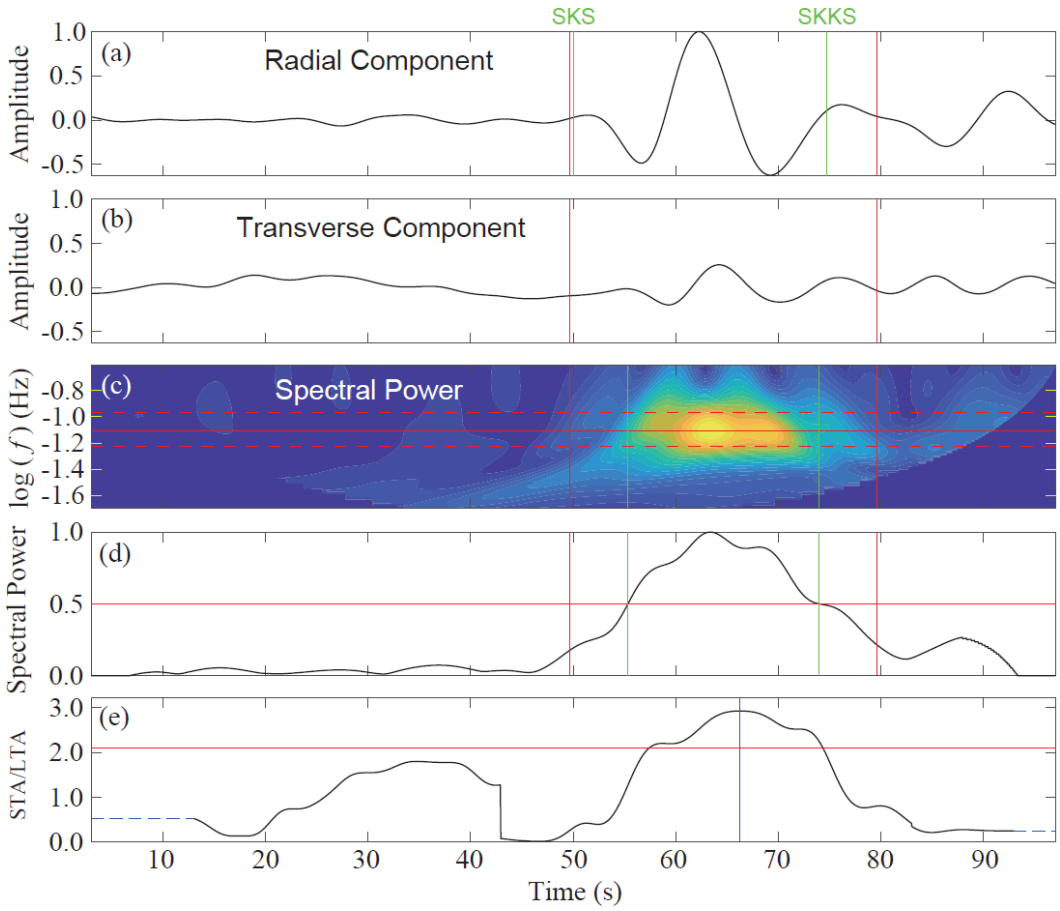

Figure 4. An example of SKS window selection using SplitRacer. (a) and (b) show normalized radial and transverse records, respectively, around the SKS arrival at station WXT (blue triangle in Figure 1) from the 24 June 2019 earthquake in New Zealand with a back azimuth of 122º. The green lines mark the theoretical SKS and SKKS arrival times corresponding to the event of interest. Red vertical lines mark the start and end times of the final window used for SI measurement. (c) Summed spectral power of the spectrogram of the radial and transverse records in (a) and (b). The red horizontal line marks the frequency of maximum spectral power, and the red dashed lines show the frequency bounds of more than 80% of the maximum. The green vertical lines mark the time window in which the summed spectral power is more than 50% of the maximum. (d) Summed spectral power over all frequencies. The green vertical lines mark the time window in which the summed spectral energy is more than 50% of the maximum. (e) STA/LTA ratio of the radial-component record used as quality check. The blue vertical line denotes the time when the STA/LTA ratio reaches its peak within the window determined in (d). The red horizontal line is the acceptance threshold of 2.1 (Link et al., 2022).

We further clean our dataset of outliers based on two criteria: (1) At a given station, SI measurements

with uncertainties σ_i larger than 1.5 times the average uncertainty $\bar{\sigma}$ for that station, i.e. $\sigma_i > 1.5\bar{\sigma}$, are removed; (2) all SI measurements at a given station are fit by a sinusoidal curve, and measurements that deviate from the sinusoidal curves by more than $2\sigma_i$ are also removed. After removing the outliers, we retain a total of 5,216 high-quality SI measurements as our final dataset for subsequent anisotropy inversion. The standard deviation of the final dataset (the average of uncertainties of all retained data) is 0.074 s. Figure 5 shows the effect on the distribution of SI measurements before and after applying the above two criteria for station WXT, which reduces the number of SI data from 184 to 61.

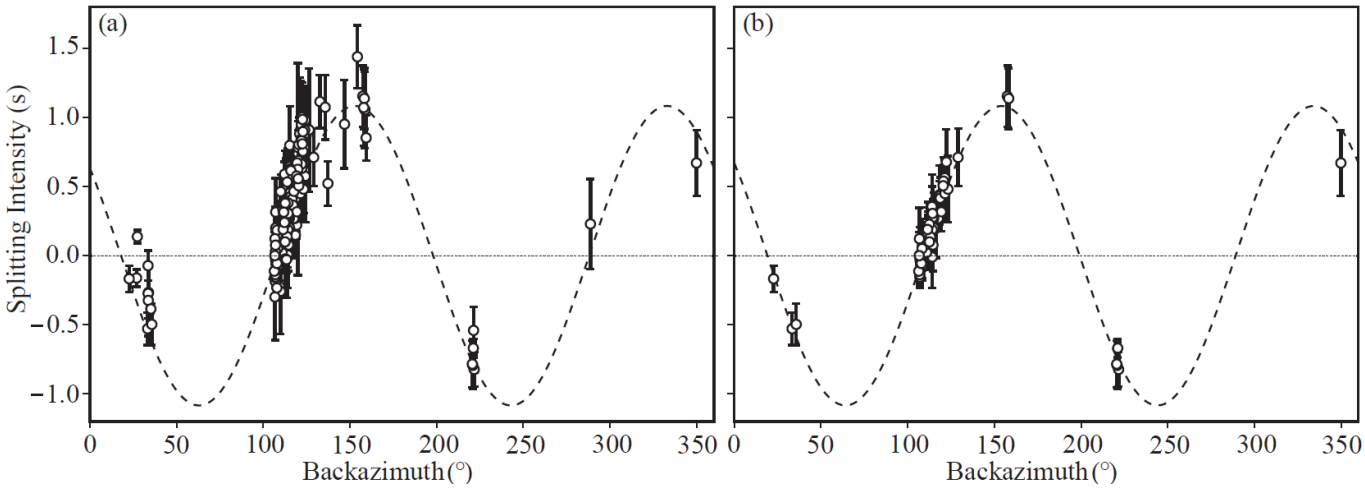

Figure 5. Variations of measured SI with event back azimuth for station WXT (blue triangle in Figure 1) before (a) and after (b) removal of SI outliers. The vertical error bars show two standard deviations ($2\sigma_i$) of individual measurements. The dashed lines represent the sinusoidal curves that best fit the measurements. According to Eq. (2), the conventional SKS splitting parameters for this station are: $\Delta t = 1.08$ s and $\theta = 109.14°$.

Based on Eq. (2), we can obtain the conventional fast-direction azimuth θ and delay time Δt at each station using all the SI measurements, and they are displayed in Figure 6. The spatial distribution of θ has a similar pattern as seen in previous studies, i.e. a generally NW-SE oriented fast axis and a nearly uniform E-W alignment of the fast-axis directions south of ~26ºN latitude.

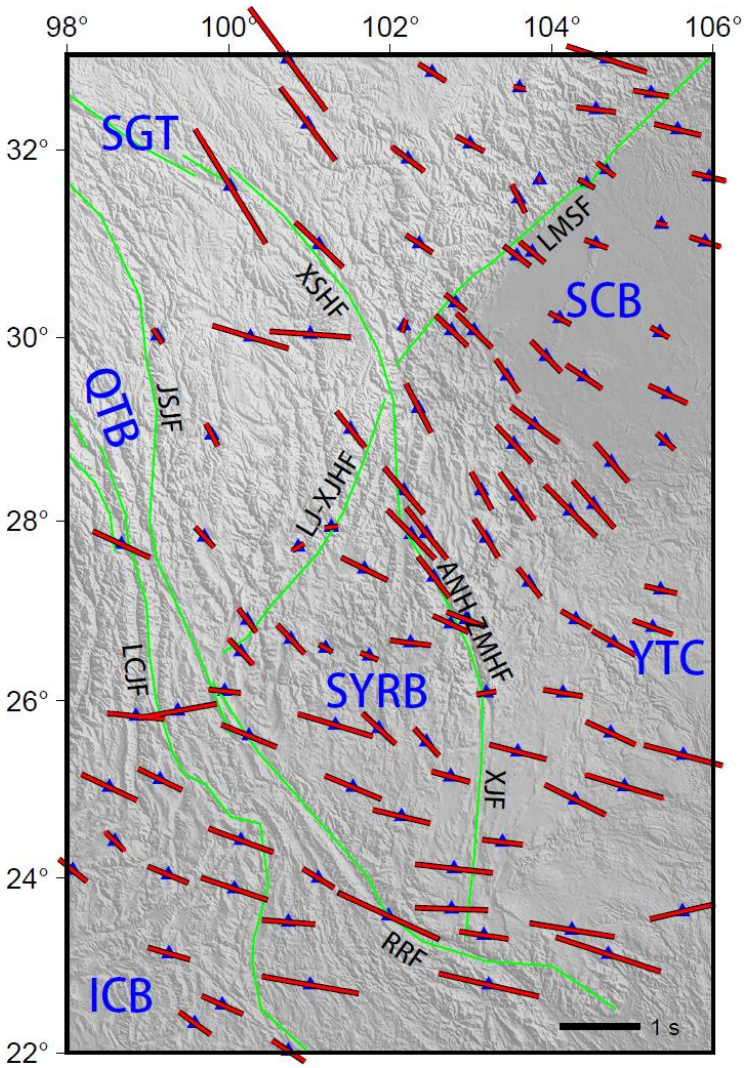

Figure 6. Black line segments show the conventional SKS fast-direction azimuths and delay times at all station obtained from the SI measurements according to Eq. (2). Red line segments are fast-direction azimuths and delay times derived from Eq. (2) based on the model-predicted SIs obtained by integrating the sensitivity kernels (see Figure 7) with the anisotropy model in Figure 12 according to Eq. (4). Names of major faults and tectonic blocks are the same as in Figure 1.

2.3 Multiscale inversion for 3D anisotropic structure

We implement the full-wave multiscale anisotropy tomography framework developed by Lin et al. (2014b). Here we briefly describe our methodology. Interested readers may consult Lin et al. (2014b) for a full description of the method.

Becker et al. (2006) pointed out that the upper-mantle anisotropy is mainly hexagonal with strongly

correlated parameters ε and γ quantifying the P- and S-wave anisotropy, respectively, and the ellipticity parameter δ. Furthermore, Zhao & Chevrot (2011) demonstrated that the SI of an SKS wave is mostly sensitive to γ, and is about 10 times larger than to the isotropic heterogeneity. This allows us to simplify the modeling of upper mantle anisotropy in two aspects: (1) it is sufficient to use a 1D reference model; and (2) the anisotropy can be described by only two parameters: the strength of anisotropy γ and the azimuth ϕ_f of the symmetry axis of anisotropy. We assume that the symmetry axis is horizontal since the sub-vertically propagating SKS waves are insensitive to the dip angle of the symmetry axis of anisotropy (Mondal & Long, 2019). Note that the anisotropy strength γ and azimuth ϕ_f are spatially varying, and the dependence of the SI on ϕ_f is nonlinear. As documented in Favier & Chevrot (2003), we can introduce two independent parameters, $\gamma_c = \gamma\cos(2\phi_f)$ and $\gamma_s = \gamma\sin(2\phi_f)$, to enable a linear relationship with the SI measurement

$$S = \iiint \left[K^S_{\gamma_c}(\boldsymbol{r})\gamma_c(\boldsymbol{r}) + K^S_{\gamma_s}(\boldsymbol{r})\gamma_s(\boldsymbol{r})\right]d\boldsymbol{r}, \tag{4}$$

where $K^S_{\gamma_c}$ and $K^S_{\gamma_s}$ are the Fréchet sensitivity kernels of the splitting intensity S to γ_c and γ_s, respectively. After obtaining γ_c and γ_s from a linear inversion, we can obtain the more familiar anisotropy parameters by utilizing the relations: $\phi_f(\boldsymbol{r}) = 0.5\tan^{-1}[\gamma_s(\boldsymbol{r})/\gamma_c(\boldsymbol{r})]$ and $\gamma(\boldsymbol{r}) = \sqrt{[\gamma_c(\boldsymbol{r})]^2 + [\gamma_s(\boldsymbol{r})]^2}$. In this study, we use PREM (Dziewonski & Anderson, 1981) as the reference model and compute the sensitivity kernels using the normal-mode summation algorithm developed by Zhao & Chevrot (2011). Examples of the Fréchet kernels for γ_c and γ_s are shown in Figure 7. Chevrot (2006) first noted the similarity between the definitions of SI in Eq. (1) and finite-frequency traveltimes (e.g. Dahlen et al., 2000; Zhao et al., 2000), which implies that the sensitivity kernels of SI to anisotropy parameters exhibit the distinct banana-doughnut shapes typical in the sensitivities of finite-frequency traveltimes to isotropic velocities, as shown in Figure 7.

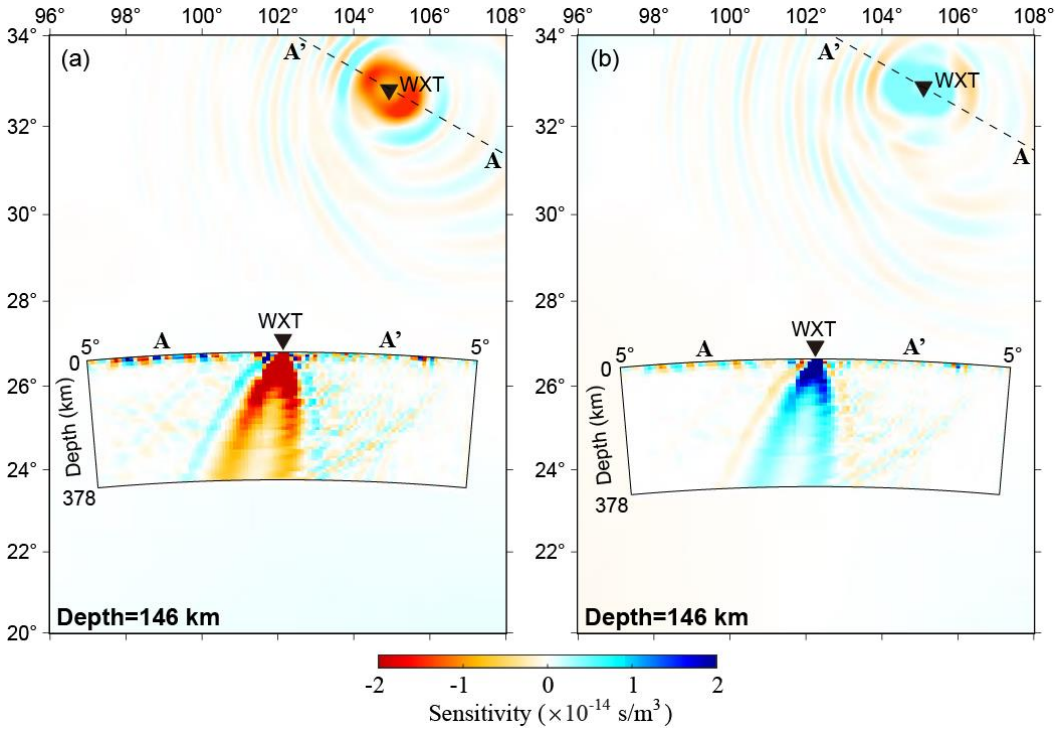

Figure 7. Examples of the sensitivity kernels of the SI to shear wave anisotropy parameters γ_c (a) and γ_s (b) shown in mapviews for the 146-km depth and in profiles (insets) along source-receiver path AA' for station WXT (blue triangle in Figure 1). The SKS wave is from the 24 June 2019 event in New Zealand with a back azimuth of 122º, and the waveforms are shown in Figure 4.

As in Lin et al. (2014b), we adopt a wavelet-based model parameterization (Chiao & Kuo, 2001) to obtain multi-scale resolutions in both sparsely- and densely-sampled regions of data coverage. The inverse problem can be expressed as:

$$(\mathbf{G}\mathbf{W}^{-1})(\mathbf{W}\mathbf{m}) = \mathbf{d}, \tag{5}$$

where $\mathbf{G}$ is the Gram matrix containing the Fréchet kernels, $\mathbf{W}$ is the 3D wavelet transform matrix, $\mathbf{m}$ is the vector containing the model parameters at spatial nodes, and $\mathbf{d}$ is the data vector of the SI measurements. In this study, we first parameterize the model by a 3D mesh with 33 × 33 nodes horizontally and 17 nodes vertically, and apply the operator $(\mathbf{W}^{-1})^T$ on each row of $\mathbf{G}$. A damped least-squares solution to the inverse problem in Eq. (5) is solved by the LSQR algorithm (Paige & Saunders, 1982), with the damping factor λ selected empirically by a series of inversion experiments (see Section 2.4), and the final

model can be obtained by an inverse wavelet transform. Readers may refer to Hung et al. (2011) for implementation details of the multi-scale parameterization. The wavelet approach achieves a higher spatial resolution where path coverage is better and a poorer resolution in less well-sampled regions, leading to results with objective and data-driven multi-scale resolution.

2.4 Resolution tests

Careful selection of the damping factor λ and objectively evaluating the resolution for a given dataset in an inversion problem are paramount to interpreting the inversion results. Thus, it is important to characterize how reliable our anisotropic models are, and to limit our interpretations to robust features that are well-resolved and well-constrained by the observations.

We present three sets of resolution tests to illustrate the selection of the optimal damping factor and the resulting resolution of our SI dataset. In each resolution test, an input model is constructed for an assumed spatial variation of anisotropy strength γ and azimuth ϕ_f. Then, the spatial distributions of γ_c and γ_s are obtained from γ and ϕ_f, and synthetic SI data for the input model are calculated for all SKS paths in our final dataset by integrating the products of the 3D sensitivity kernels $K_{\gamma_c}^S$ and $K_{\gamma_s}^S$ with γ_c and γ_s according to Eq. (4). Gaussian noise with the same standard deviation as our final inversion dataset (0.074 s) is added to the synthetic SI data. We first perform a series of tests using checkerboards of two different sizes (1º x 1º and 1.5º x 1.5º) with horizontally alternating azimuthal angles of fast axes $\phi_f = 90^\circ$ and $\phi_f = 45^\circ$ but a fixed anisotropy strength $\gamma = 4\%$. Figure 8 shows the input and recovered models for different values of the damping factor λ at a depth of 55 km for the 1º x 1º checkerboard test. The effect of damping factor on the anisotropy pattern in the inversion result is obvious. The recovery results suggest an optimal damping factor of $\lambda = 4$, and the checkerboard pattern is well-resolved in most parts of the study area except in the northwest and southeast corners where stations are more sparse. Results for the recovered models at different depths as well as for 1.5º x 1.5º checkerboards are presented in Figures

S1 and S2 in Supporting Information. Results of similar tests with alternating orthogonal azimuths of the fast axis are presented Figures S3 and S4 in Supporting Information.

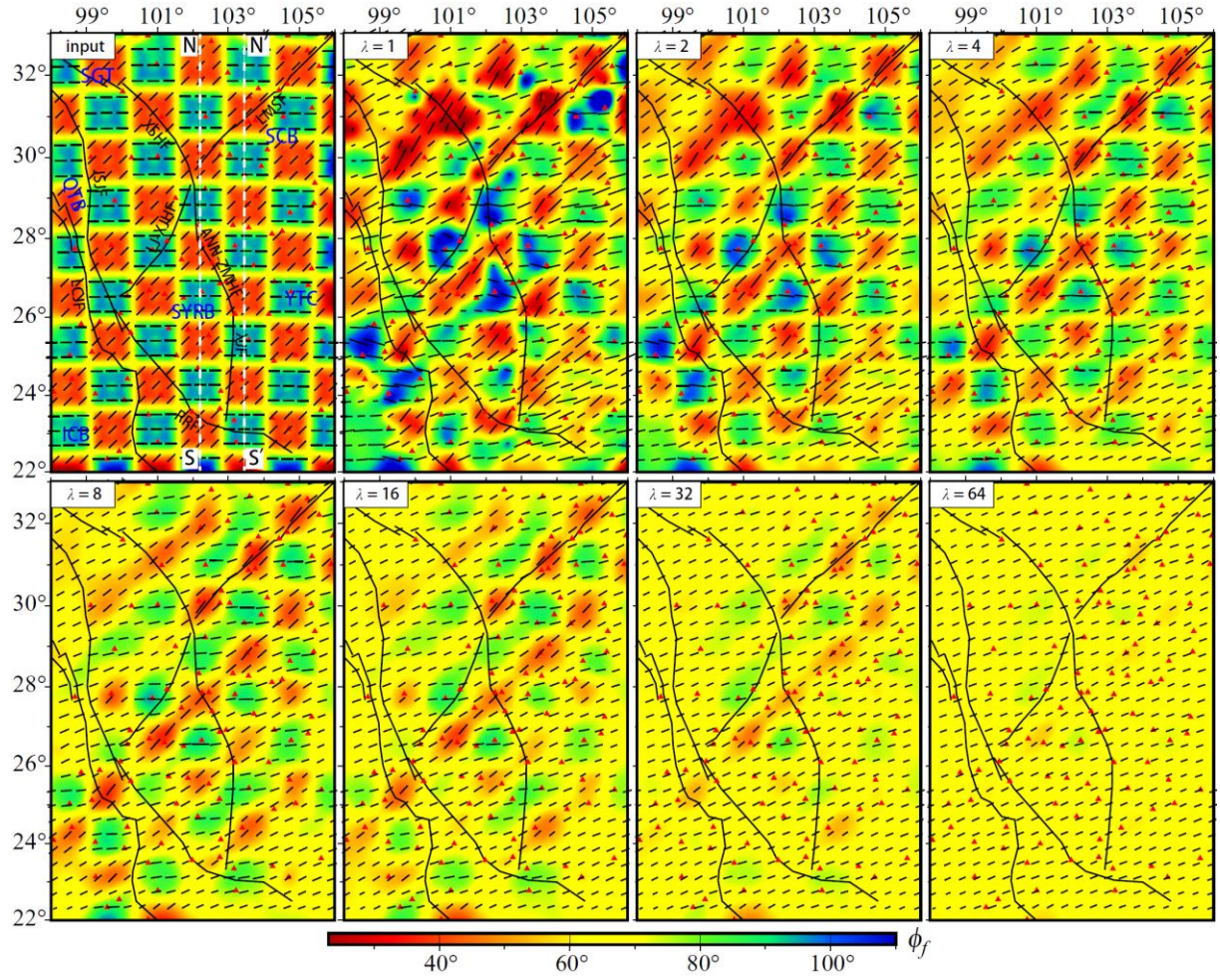

Figure 8. Resolution tests for the azimuth of symmetry axis using 1º x 1º checkerboard. (Top-left) The input model has horizontally alternating azimuthal angles of fast axes $\phi_f = 90^\circ$ and $\phi_f = 45^\circ$ shown by both the color and the directions of the line segments, and a fixed anisotropy strength $\gamma = 4\%$ represented by the lengths of the line segments. The two white dashed lines show the locations of profiles NS and N'S' in Figure 11. The other panels show the recovered models at a depth of 55 km for different damping factors λ. We choose $\lambda = 4$ as the optimal value for the damping factor (top-right panel). Red triangles show locations of stations used.

In the second set of tests, we use input checkerboard models with a fixed azimuthal angle of symmetry axis $\phi_f = 22.5^\circ$ but alternating perturbations of anisotropy strength of $\delta\gamma = \pm 3\%$ relative to a

background anisotropy strength of $\gamma = 4\%$. Figure 9 shows the recovery results at the depth of 55 km using different damping factors for the 1° x 1° input checkerboard model. Results for the recovered models at different depths as well as for 1.5° x 1.5° checkerboards are presented in Figures S5 and S6 in Supporting Information.

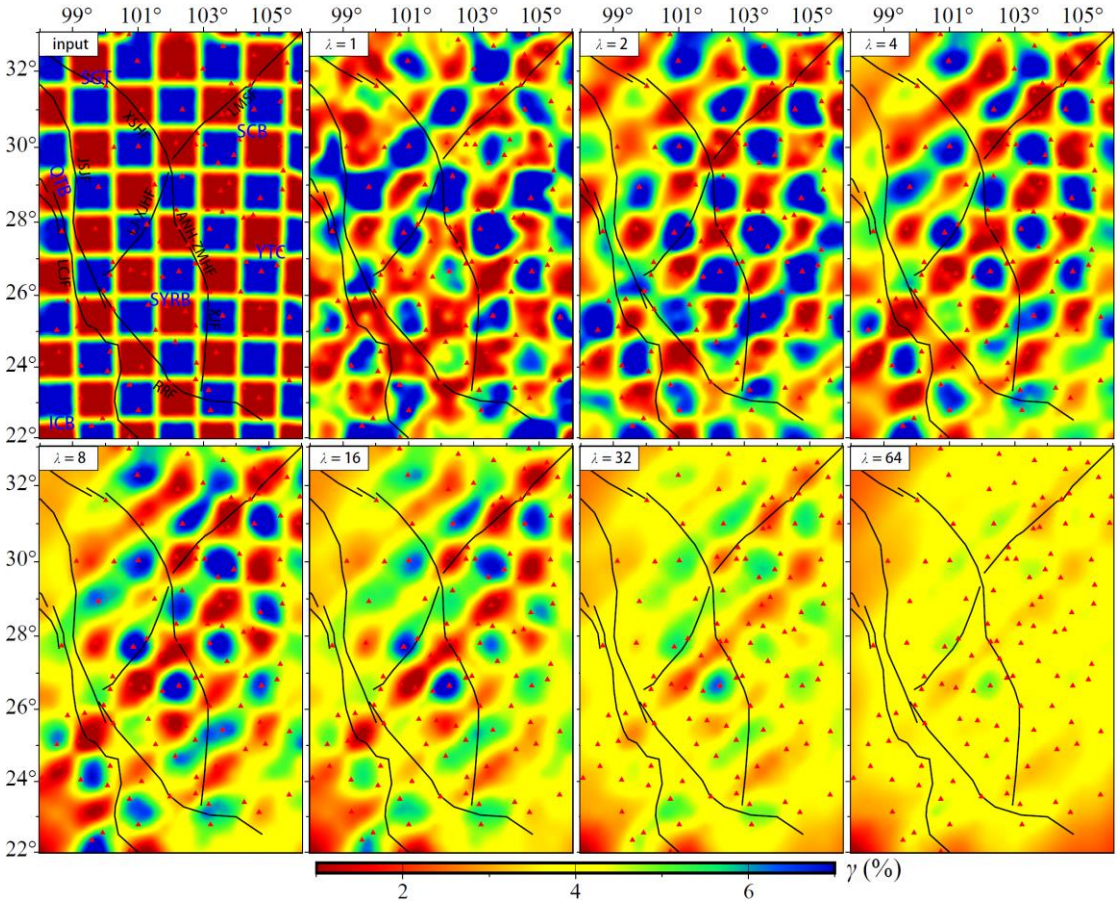

Figure 9. Resolution test using 1° x 1° checkerboard. (Top-left) The input model has horizontally alternating anisotropy strengths shown by the colors representing perturbations of $\delta\gamma = \pm 3\%$ relative to a background anisotropy strength of $\gamma = 4\%$, and a fixed azimuthal angle of symmetry axis $\phi_f = 22.5^{\circ}$. The other panels show the recovered models at a depth of 55 km for different damping factors λ. We choose $\lambda = 4$ as the optimal value for the damping factor (top-right panel).

The tests in Figures 8 and 9 both show that the damping factor of $\lambda = 4$ yields the best resolved checkerboard pattern. For convenience, resolution test results at different depths for damping factor $\lambda = 4$ are collected and displayed in Figure 10.

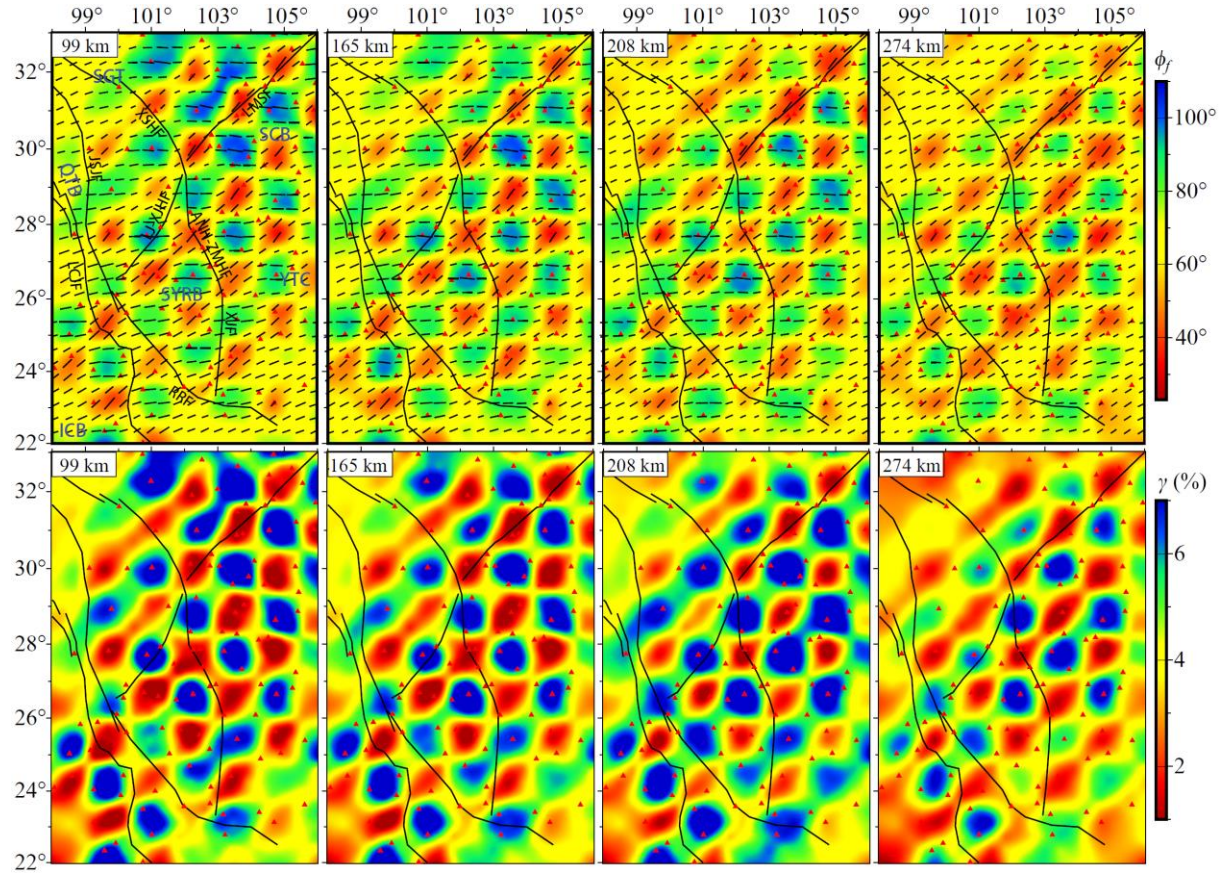

Figure 10. Resolution test using 1° x 1° checkerboard with damping factor $\lambda = 4$. (Upper panels) Recovered model at the depths of 99 km, 165 km, 208 km and 274 km for an input model having horizontally alternating azimuthal angles of fast axes $\phi_f = 90^\circ$ and $\phi_f = 45^\circ$ with a fixed anisotropy strength $\gamma = 4\%$. The input model and the recovered model at 55-km depth are shown in Figure 8. (Lower panels) Recovered model at the depths of 99 km, 165 km, 208 km and 274 km for an input model with horizontally alternating anisotropy strengths of $\gamma = 1\%$ and $\gamma = 7\%$ (perturbations of $\delta\gamma = \pm 3\%$ relative to a background anisotropy strength of $\gamma = 4\%$) with a fixed azimuthal angle of symmetry axis $\phi_f = 22.5^\circ$. The input model and the recovered model at 55-km depth are shown in Figure 9.

The third set of tests is intended to probe the depth resolution of our SI dataset with full-waveform anisotropy tomography. We use input models with a fixed anisotropy strength of $\gamma = 4\%$ but several layers of alternating azimuthal angles of symmetry axes. Figure 11 shows the recovery results for a 4-layer input model along a north-south vertical cross-section (cross-section NS in the top-left panel of Figure 8) for different damping factors.

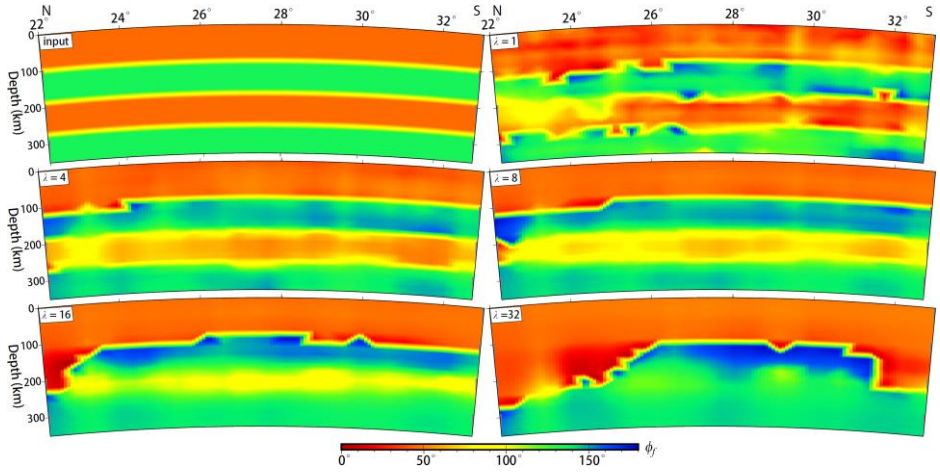

Figure 11. Resolution tests for an input model with 4 layers of alternating azimuthal angles of symmetry axes $\phi_f = 45^\circ$ and $\phi_f = 135^\circ$ but a fixed anisotropy strength of $\gamma = 4\%$. Shown here are the input model (top-left panel) and recovered models for different damping factors λ along the north-south cross-section NS through the middle of the study region (see top-left panel in Figure 8). The optimal damping is $\lambda = 4$ (middle-left panel).

Recovered models along another profile as well as for a 2-layer input model are presented in Supporting Information (Figures S7-S10). These results also suggest an optimal damping factor of $\lambda = 4$. Based on all the resolution test results, we determine $\lambda = 4$ to be the optimal damping factor for the SI data inversions in this study. It should be noted that the noise level in the SI measurements can affect the choice of the damping factor. The higher the noise level, the larger the damping factor (see the tests in Figures S11–S14).

The above resolution tests demonstrate that with the available distributions of seismic stations and teleseismic earthquakes, our SKS wave SI dataset can resolve reasonably well the shear-wave azimuthal anisotropy with a horizontal dimension of 1º x 1º and a vertical thickness of ~100 km in the main part of the study region. Near the western border and in the SE corner, the resolution is poor due to larger station spacing and fewer crossing SKS ray paths.

3 Result

As stated in Section 2.2, our final dataset contains 5,216 SI measurements at 111 permanent seismic

stations from 470 events, which are used to invert for the 3D azimuthal anisotropy structure of the study region. Figure 12 displays our inverted model at five representative depths. The azimuths of fast axis along four vertical profiles are shown in Figure 13.

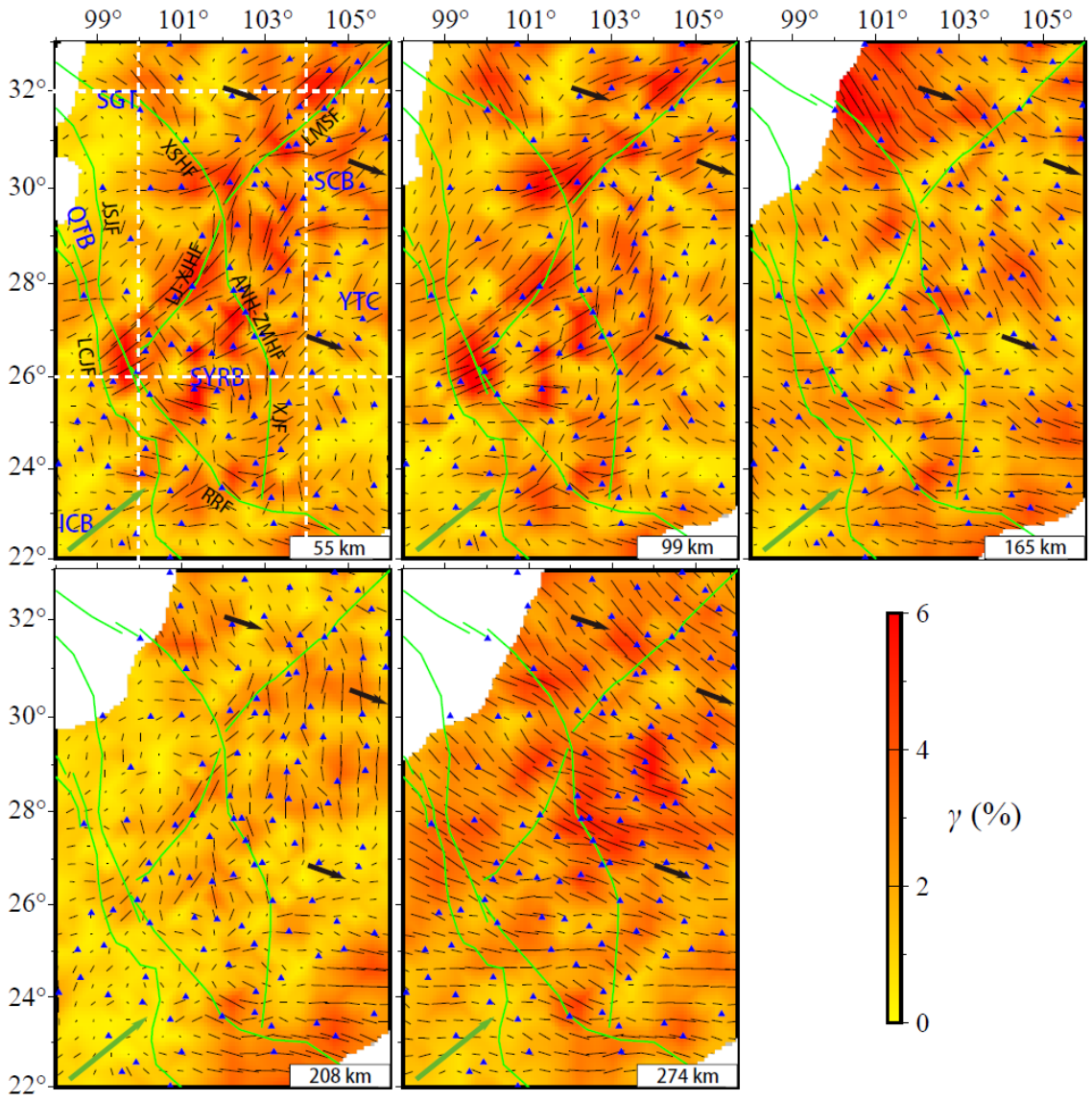

Figure 12. Three-dimensional anisotropic model for the SE margin of Tibetan Plateau at 55 km, 99 km, 165 km, 208 km and 274 km depths. The anisotropy strength and the azimuth of the fast axes are shown by the background color and the black line segments, respectively. The lengths of the line segments are proportional to the anisotropy strength. The black and green arrows denote the absolute plate motion (APM) of the Eurasian and Indian plates, respectively, according to the model NNR-MORVEL56 (Argus et al., 2011). The white dashed lines show locations of the profiles shown in Figure 13. Names of major

faults and tectonic blocks are the same as in Figure 1. Blue triangles show locations of stations used. Regions in which the recovery errors are above 20% are mask out. The recovery error is defined by $E = \left(|\phi_f - \tilde{\phi}_f|/90°\right) \times 100\%$, where $\tilde{\phi}_f$ and ϕ_f are the input and recovered azimuthal angles in the resolution tests in Figures 8 and 10.

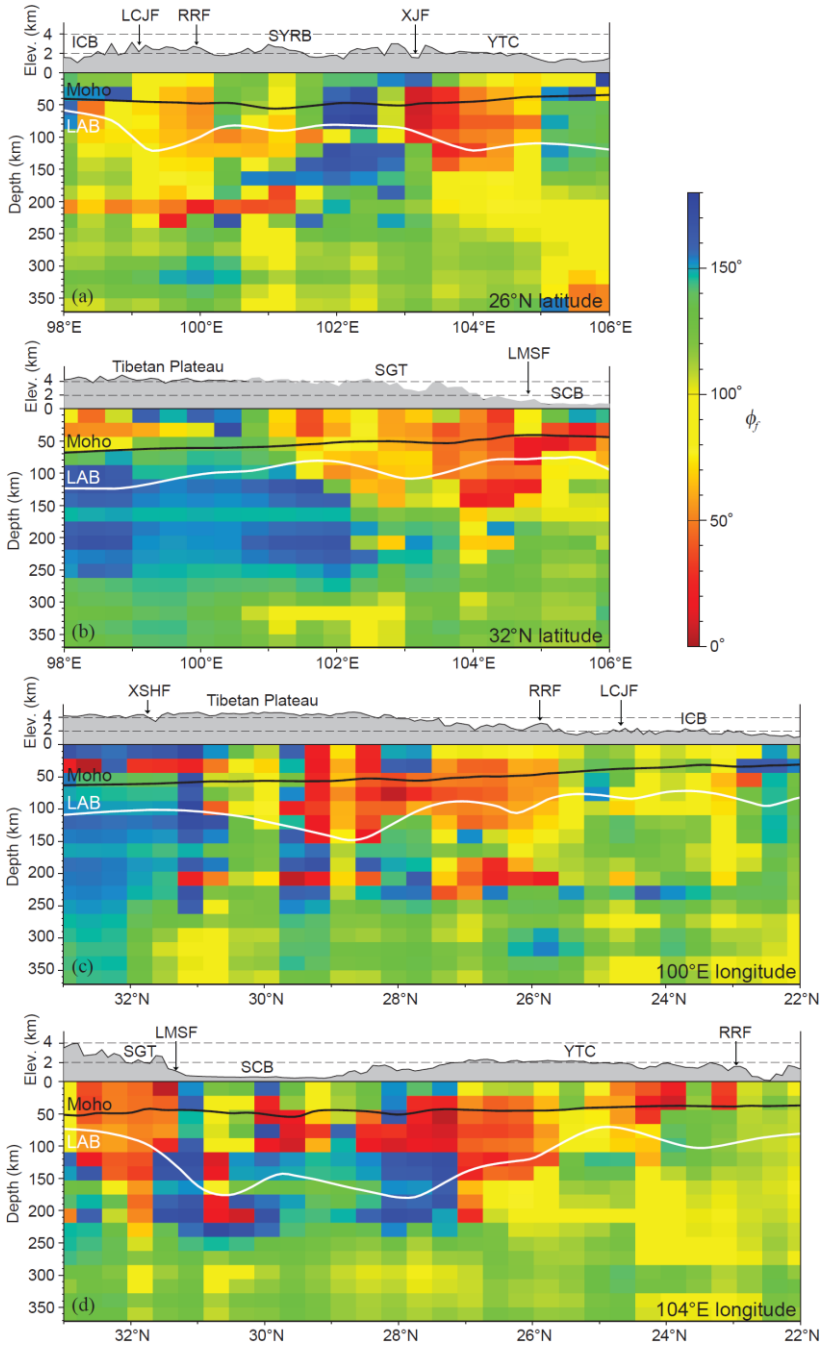

Figure 13. Vertical profiles of the azimuths of fast axis in our 3D anisotropy model along (a) 26ºN latitude, (b) 32ºN latitude, (c) 100ºE longitude and (d) 104ºE longitude. The azimuths of the fast axis are shown by

the background color. Note that red (~0º) and blue (~180º) colors both indicate nearly N-S fast axis, whereas yellow color indicates nearly E-W fast axis. Moho and lithosphere-asthenosphere boundary (LAB) are depicted by thick black and white lines, respectively. Names of major faults and tectonic blocks are the same as in Figure 1.

As a first check of the inversion result, we calculate the model-predicted conventional SKS splitting time Δt and fast-direction azimuth θ by integrating the anisotropy model (Figure 12) with sensitivity kernels (Figure 7) according to Eq. (4) and compare with observations. The comparison in Figure 6 shows excellent agreement between the model-predicted splitting parameters with observations at all stations.

We also carry out a recovery test for our inversion result, in which we use the model in Figure 12 as the input model and calculate the synthetic SI data, then invert them using the same model discretization and damping factor as in the inversion of the real data. The comparison in Figure 14 shows that the output model strongly resembles the input model at all depths. The synthetic inversion successfully reproduces all the major features of the input model.

4 Discussion

4.1 Comparison with previous results

SKS splitting observation has been widely used to investigate the upper mantle anisotropy in the SE margin of Tibetan Plateau (e.g., Lev et al., 2006; Flesch et al., 2005; Wang et al., 2008; Shi et al., 2012; Chang et al., 2015; Yang et al., 2018; Liu et al., 2020; Huang & Chevrot, 2021; Li et al., 2021). In Figure 15, we compare our splitting result with those of Chang et al. (2015) and Liu et al. (2020) whose SKS splitting data are available from the Shear Wave Splitting Product Query website (http://ds.iris.edu/spud/swsmeasurement). At most stations, predictions by our model are consistent with both studies. Major differences occur at two stations at the southern tip of SCB (highlighted by the blue ellipse in Figure 15), where anomalously large splitting times can be seen in the results of Liu et al. (2020), shown by the red line segments. There are also discrepancies in both delay time and fast-axis azimuth at a few stations across the LJ-XJHF (highlighted by the red ellipses in

Figure 15) where Chang et al. (2015) reported large splitting times and nearly N-S fast axes, whereas our model predicts moderate-to-small splitting times and more E-W orientation of fast axes. Note that a strictly quantitative comparison of different studies is difficult due to differences in earthquake and window selections, data processing and frequency bands used in the measurement of SKS splitting parameters.

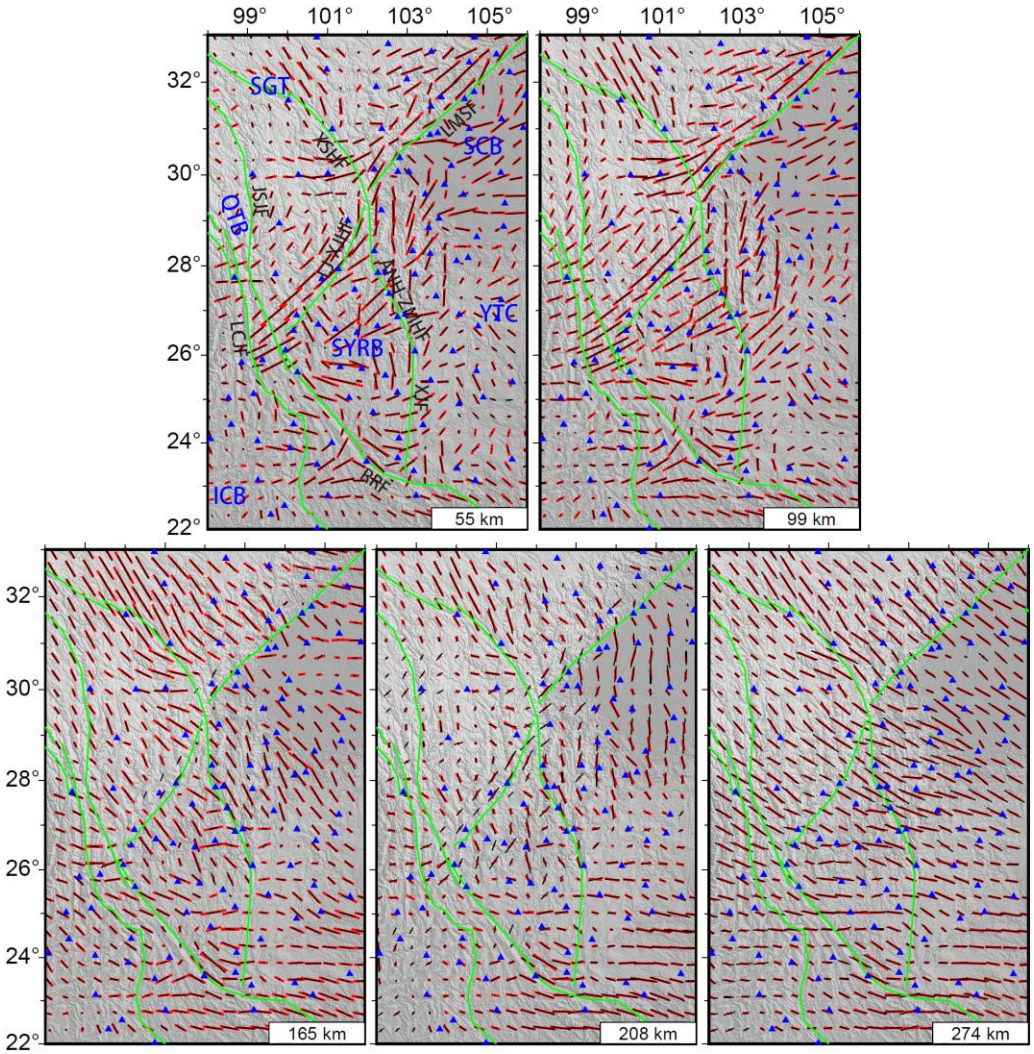

Figure 14. Result of the recovery test. The recovered and input anisotropic models are compared at five depths marked at the bottom-right corner in each panel. Black and red line segments denote the directions of fast axes in the input and recovered models, respectively, and their lengths indicates the anisotropy strength. Names of major faults and tectonic blocks are the same as in Figure 1. Blue triangles show locations of stations used.

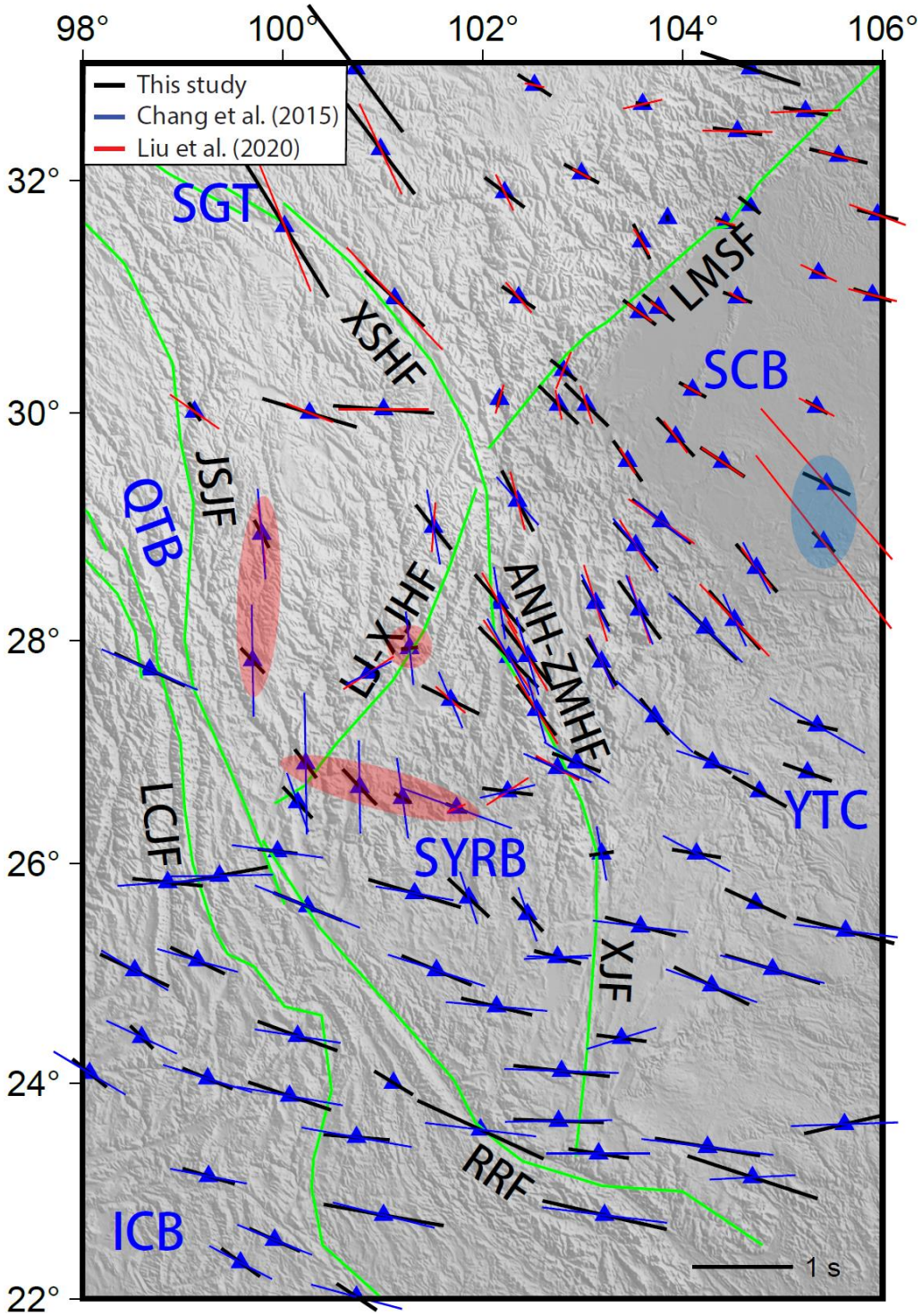

Figure 15. Comparison of SKS splitting times and fast axis directions predicted by our anisotropy model (Figure 12) with previous studies. Black line segments are results from the present study, whereas blue and red line segments show results from Chang et al. (2015) and Liu et al. (2020), respectively. Blue and red ellipses highlight stations where there are large discrepancies in splitting parameters between this study and Liu et al.

(2020) and Chang et al. (2015), respectively. Names of major faults and tectonic blocks are the same as in Figure 1.

Depth variation of anisotropy can also be investigated by surface-wave tomography studies (e.g. Montagner & Nataf, 1986; Debayle et al., 2005; Lin et al., 2011). Bao et al. (2020) and Zhang et al. (2023) used Rayleigh-wave dispersion curves measured from ambient noise and teleseismic earthquakes to invert for the azimuthal anisotropy in the SE margin of Tibetan Plateau. In general, both surface-wave results show a lower anisotropy strength of 2−3% with smoother spatial variation patterns than our model obtained from SKS splitting intensity. At the relatively shallow depths (~55 km) in the vicinity of the LMSF and LJ-XJHF, all models exhibit fast axes nearly parallel to the fault zones. Surface-wave tomography acquires depth resolution from different depth distributions of sensitivity of surface waves of different frequencies, but its horizontal resolution is limited due to the horizontal averaging of horizontally propagating surface waves. In addition, almost all surface-wave tomography studies use fundamental Rayleigh waves, which also limits the depth resolution. On the other hand, our fullwave SI inversion uses nearly vertically propagating SKS waves, which acquires spatial resolution from the 3D sensitivity kernels (Figure 7) with higher resolution horizontally than vertically. Therefore, discrepancies between models obtained by surface-wave dispersion and SKS SI can be expected given the current station distribution and available data.

4.2 Overall variation of shear-wave anisotropy

Our anisotropy model exhibits an overall anisotropy strength γ of up to 6% in the lithosphere and asthenosphere. Both the strength and fast-axis show strong lateral and vertical variations (Figures 12 and 13). Within the lithosphere (depths of 55 km and 99 km), the anisotropy is strong in the vicinity of the LMSF and LJ-XJHF, the major fault zones in the region that form the boundary between the Tibetan Plateau and the YTC. At greater depths in the asthenosphere (e.g. 274 km), the entire region exhibits strong anisotropy with a largely NW-SE fast axis (predominantly green color in the lower parts in Figure

13), parallel to the direction of GPS observed surface velocity (Figure 1) and the APM (black arrows in Figure 12), and turns to more E-W south of ~26ºN. At intermediate depths (165 km and 208 km), the anisotropy is highly variable, both in strength and direction of symmetry axis. Therefore, our model shows an apparent decoupling of lithosphere and asthenosphere deformation in the SE margin of Tibetan Plateau, consistent with previous studies (e.g. Flesch et al., 2005).

Most previous studies have reported two major features in the SKS splitting pattern in the region: an overall NW-SE fast axis and an E-W alignment of fast axes south of ~26ºN latitude (e. g., Lev et al., 2006; Wang et al., 2008; Chang et al., 2015; Huang & Chevrot, 2021), as shown in Figures 6 and 15. Our model shows that this relatively simple splitting pattern observed at seismic stations on the surface is a manifestation of the vertical averaging of complex variation of anisotropy over lithospheric and asthenospheric depths. For instance, along the LMSF, the fast axes in the lithospheric depths (e.g. 55 km and 99 km) are mainly oriented NE-SW with relatively high anisotropy strength, but change to NW-SE in the asthenosphere. As a result, we observe relatively small SKS splitting times (< 0.5 s) with a NW-SE fast axis at the surface. On the other hand, the moderate SKS splitting times (1 s or less) and E-W alignment of fast axes south of ~26ºN are resulted primarily from a strong E-W azimuthal anisotropy (green and yellow colors south of 26ºN and below the LAB in Figures 13c and 13d) generated by an E-W asthenospheric flow due to the eastward subduction of the Indian Plate under Myanmar (e.g. Yang et al., 2022). Regional variation of lithospheric and asthenospheric contributions to anisotropy leads to small but discernable differences in SKS splitting observations. For example, under the SYRB, the anisotropy in the lithosphere between 24ºN and 26ºN is relatively strong (55 km and 99 km depths in Figure 12) with different orientations of fast axes. The vertical integration of lithospheric and asthenospheric anisotropy results in horizontally variable SKS splitting times and fast axes observed at seismic stations on the surface, as shown by the stations in SYRB in Figures 6 and 15. In the rest of the study region south of 26ºN, the asthenospheric contribution dominates, and the surface

459 SKS splitting parameters exhibit relatively uniform E-W fast axes.

460 **4.3 The Songpan-Ganzi Terrane**

461 In our study region, the SGT is bounded by the JSJF in the southwest and LMSF and LJ-XJHF in the
462 southeast (Li et al., 2021). In the eastern margin of the SGT, the eastward expansion of the Tibetan Plateau
463 is blocked by the SCB, part of the YTC. Our model shows two distinct types of anisotropy. In the area far
464 away from the LMSF, the anisotropy is moderate to strong (3–6%) with NW-SE fast axes in both
465 lithosphere and asthenosphere (light blue and green colors under Tibetan Plateau in Figures 13b and 13c),
466 parallel to the GPS surface velocity (Figure 1), the regional APM direction (black arrows in Figure 12)
467 and the asthenospheric flow, suggesting a vertical coupling of deformation there, in agreement with Flesch
468 et al. (2005). The NW-SE anisotropy in the SGT is consistent with previous tomography results from
469 Rayleigh waves (Legendre et al., 2015; Bao et al., 2020) and Pn waves (Lei et al., 2014). However, in the
470 area near the LMSF, the fast axis in the lithosphere (e.g. 55 km and 99 km depths) becomes NE-SW,
471 parallel to the proposed lithospheric material flow as a result of the resistance of SCB to the eastward
472 expansion of the Tibetan Plateau at LMSF. Near the LMSF, lithospheric material of the SGT appears to
473 diverge at ~102º longitude, going in opposite directions (NE and SW). In the asthenosphere, the fast axis
474 returns to NW-SE, consistent with the regional APM. The relatively sharp turn of the fast axis in the
475 lithosphere from SE-NW to NE-SW at the southern tip of SGT is a clear evidence for the redirection of
476 the lithospheric flow from eastward to southward in the SE margin of Tibetan Plateau.

477 **4.4 The Yangtze Craton**

478 The YTC is a Precambrian continental block which was accreted to the North China Craton in the Triassic. Our
479 study region covers the western margin of the YTC, namely the SCB and SYRB, and our model shows
480 that the anisotropy in the region varies significantly both horizontally and vertically, as a result of the
481 complex geodynamic evolution of the YTC involving multiple rounds of lithospheric reactivation, such

as the Permian-Triassic Emeishan flood basalt eruption (e.g. Xu et al., 2001), as well as interactions with surrounding tectonic blocks. In our model, the SCB exhibits a moderate anisotropy with a NE-SW orientation near the LMSF at shallow depths (e.g. 55 km and 99 km depths in Figure 12 and yellow and red colors under LMSF in Figure 13b), presumably the effect of a dominant shearing in the vicinity of the LMSF by the moving SGT lithosphere in NE and SW directions. Further east, E-W compression gradually takes over the NE-SW shear at shallow depths, and the fast axis of anisotropy turns to more E-W (e.g. 55 km, 99 km and 165 km). This turn of anisotropy from NE-SW to more E-W away from the LMSF has also been observed in surface-wave studies (e.g. Zhang et al., 2023). At greater depths in the lithosphere (208 km in Figure 12 and red and blue colors under SCB in Figure 13d), the anisotropy under the SCB becomes nearly N-S, which is consistent with a frozen anisotropy in the lithosphere generated by the mantle flow in the Cenozoic (Li et al., 2021) without being modified by the SGT-SCB block interaction at shallower depths. At asthenospheric depths (274 km), the anisotropy is largely aligned with the regional APM.

The anisotropy under the SYRB appears to be continuous across the ANH-ZMHF and XJF, suggesting that both fault systems are crustal boundaries where the SYRB is escaping in the SE direction. In the lithosphere (55 km and 99 km under SYRB and above 208 km depth east of ANH-ZMHF between the SCB and 26ºN), the anisotropy has a complex pattern of relatively small-scale horizontal variations of fast axes, perhaps a result of multiple phases of lithospheric reactivations that have modified the previously frozen anisotropy. In the asthenosphere (> 100 km depth in SYRB and > 200 km between the SCB and 26ºN), the anisotropy largely follows the direction of the regional APM or mantle flow. Around 208-km depth, the azimuthal anisotropy south of the SCB is very weak, which may indicate a more complex local mantle flow pattern due to the regionally predominant NW-SE mantle flow being disturbed by the root of the YTC lithosphere. South of 26ºN, the anisotropy under the YTC returns to largely parallel to the direction of APM.

5 Conclusions

In this study, we have carried out fullwave multiscale tomography to obtain a 3D model for the shear-wave anisotropy in the SE margin of Tibetan Plateau. A total of 5,216 high-quality SKS splitting intensities are obtained from the broadband records of 470 teleseismic events at 111 permanent stations after a series of quality control measures. In conjunction with the 3D sensitivity kernels and a wavelet-based parameterization, the splitting intensities are inverted to achieve a data-driven multi-scale resolution to anisotropy structure in the upper mantle.

The vertical variation of the anisotropy in our result indicates that the lithospheric and asthenospheric deformations are decoupled in the SE margin of the Tibetan Plateau. On the other hand, the anisotropy appears to be vertically consistent under the Songpan-Ganzi Terrane, suggesting a coupling of the deformations in the lithosphere and asthenosphere in the interior of the Tibetan Plateau. It is worthwhile to point out that the vertical resolution is limited due to the nearly vertical propagation of the SKS waves. As a result, the Moho discontinuity and crustal anisotropy are poorly resolved in our anisotropy model.

The strength of anisotropy in our model is spatially variable and can reach 6%, with strongest anisotropy in the asthenosphere presumably due to large-scale and relatively steady mantle flow, and in the lithosphere in the vicinity of the Longmenshan Fault and Lijiang-Xiaojinhe Fault, probably due to large shearing effect generated by the relative movement between the Songpan-Ganzi Terrane and the Sichuan Basin.

The azimuth of the fast axis of anisotropy in the asthenosphere largely follows the direction of regional absolute plate motion or mantle flow, i.e. mostly southeastward beneath the Songpan-Ganzi Terrane and the Yangtze Craton and nearly east-west south of 26^{o}N latitude. In the lithosphere, however, the fast axis is highly variable. In the Sichuan Basin, the frozen anisotropy dominates in the deep lithosphere; whereas at shallower depths, the anisotropy is modified by the interaction with the Songpan-Ganzi Terrane into southeastward in the

vicinity of the Longmenshan Fault and nearly east-west further east. In the Sichuan-Yunnan Rhombic Block and east of the Anninghe-Zemuhe Fault, the azimuth of the fast axis of anisotropy exhibits complex spatial pattern due to multiple phases of lithospheric reactivation. The vertical integration of the contributions from complex lithospheric anisotropy and relatively uniform asthenospheric anisotropy gives rise to the seemingly simple pattern of conventional SKS splitting parameters observed at the surface. Our 3D model of azimuthal anisotropy provides important new insights into the lithospheric and asthenospheric dynamics in the SE margin of Tibetan Plateau.

Acknowledgments

We sincerely thank the two anonymous reviewers for their critical reviews and constructive comments which greatly helped improve the manuscript. This work has been supported by the National Natural Science Foundation of China (NSFC Grants U1939202 and 41974046). Y.L. has been supported by the 68th China Postdoctoral Science Foundation under Grant 2020M680205. Most of the figures are generated using the Generic Mapping Tools (Wessel et al., 2019, https://www.generic-mapping-tools.org).

Open Research

The raw waveform data, the measured splitting intensities as well as the obtained anisotropic model can be accessed at Lin, Y., & Zhao, L. (2024).

References

Argus, D. F., Gordon, R. G., & DeMets, C. (2011). Geologically current motion of 56 plates relative to the no-net-rotation reference frame. *Geochemistry, Geophysics, Geosystems*, *12*(11). doi: 10.1029/2011GC003751

Bao, X., Song, X., Eaton, D. W., Xu, Y., & Chen, H. (2020). Episodic lithospheric deformation in eastern Tibet inferred from seismic anisotropy. *Geophysical Research Letters*, 47(3). doi: 10.1029/2019gl085721

Becker, T. W., Chevrot, S., Schulte-Pelkum, V., & Blackman, D. K. (2006). Statistical properties of seismic anisotropy predicted by upper mantle geodynamic models. *Journal of Geophysical Research: Solid Earth*, 111(B8). doi: 10.1029/2005JB004095

Cai, Y., Wu, J., Fang, L., Wang, W., & Yi, S. (2016). Crustal anisotropy and deformation of the southeastern margin of the Tibetan Plateau revealed by Pms splitting. *Journal of Asian Earth Sciences*, 121, 120–126. doi: 10.1016/j.jseaes.2016.02.005

Chang, L.-J., Ding, Z.-F., & Wang, C.-Y. (2015). Upper mantle anisotropy beneath the southern segment of north-south tectonic belt, China. *Chinese Journal of Geophysics (in Chinese)*, 58(11), 4052–4067. doi: 10.6038/cjg20151114

Chevrot, S. (2000). Multichannel analysis of shear wave splitting. *Journal of Geophysical Research: Solid Earth*, 105(B9), 21579–21590. doi: 10.1029/2000JB900199

Chevrot, S. (2006). Finite-frequency vectorial tomography: a new method for high-resolution imaging of upper mantle anisotropy. *Geophysical Journal International*, 165(2), 641–657. doi: 10.1111/j.1365-246X.2006.02982.x

Chiao, L. Y., & Kuo, B. Y. (2001). Multiscale seismic tomography. *Geophysical Journal International*, 145(2), 517-527. doi: 10.1046/j.0956-540x.2001.01403.x

Dahlen, F., Hung, S.-H., & Nolet, G. (2000). Fréchet kernels for finite-frequency travel- times—I. Theory. *Geophysical Journal International*, 141(1), 157-174. doi: 10.1046/j.1365-246X.2000.00070.x

Debayle, E., Kennett, B., & Priestley, K. (2005). Global azimuthal seismic anisotropy and the unique plate-motion deformation of Australia. *Nature*, 433, 509-512.

Dziewonski, A. M., & Anderson, D. L. (1981). Preliminary reference Earth model, *Physics of the Earth and Planetary Interior,* 25**,** 297–356.

Favier, N., & Chevrot, S. (2003). Sensitivity kernels for shear wave splitting in transverse isotropic media. *Geophysical Journal International*, 153(1), 213–228. doi: 10.1046/j.1365-246X.2003.01894.x

578 Flesch, L. M., Holt, W. E., Silver, P. G., Stephenson, M., Wang, C.-Y., & Chan, W. W. (2005).
579 Constraining the extent of crust–mantle coupling in central Asia using GPS, geologic, and shear wave
580 splitting data. *Earth and Planetary Science Letters*, 238(1-2), 248-268. doi:
581 10.1016/j.epsl.2005.06.023
582 Han, C., Xu, M., Huang, Z., Wang, L., Xu, M., Mi, N., Yu, D., Guo, T., Wang, H., Hao, S., Tia, M., &
583 Bi, Y. (2020). Layered crustal anisotropy and deformation in the SE Tibetan Plateau revealed by
584 Markov- Chain-Monte-Carlo inversion of receiver functions. *Physics of the Earth and Planetary*
585 *Interiors*, 306 , 106522. doi: 10.1016/j.pepi.2020.106522
586 Hu, J., Su, Y., Zhu, X., & Chen, Y. (2005). S-wave velocity and Poisson's ratio structure of crust in
587 Yunnan and its implication. *Science in China Series D: Earth Sciences*, 48(2), 210–218. doi:
588 10.1360/03yd0062
589 Huang, J., Zhao, D., & Zheng, S. (2002). Lithospheric structure and its relationship to seismic and volcanic
590 activity in southwest China. *Journal of Geophysical Research: Solid Earth*, 107(B10), ESE–13. doi:
591 10.1029/2000JB000137
592 Huang, P., Gao, Y., & Xue, B. (2022). Advances in the deep tectonics and seismic anisotropy of the
593 Lijiang-Xiaojinhe fault zone in the Sichuan-Yunnan block, southwestern China. *Earthquake*
594 *Research Advances*, 2(1), 100116. doi: 10.1016/j.eqrea.2022.100116
595 Huang, R., Wang, Z., Pei, S., & Wang, Y. (2009). Crustal ductile flow and its contribution to tectonic
596 stress in Southwest China. *Tectonophysics*, 473(3-4), 476–489. doi: 10.1016/ j.tecto.2009.04.001
597 Huang, Z., & Chevrot, S. (2021). Mantle dynamics in the SE Tibetan Plateau revealed by teleseismic
598 shear-wave splitting analysis. *Physics of the Earth and Planetary Interiors*, 313, 106687. doi:
599 10.1016/j.pepi.2021.106687
600 Huang, Z., Wang, L., Xu, M., & Zhao, D. (2018). P wave anisotropic tomography of the SE Tibetan
601 Plateau: Evidence for the crustal and upper-mantle deformations. *Journal of Geophysical Research:*
602 *Solid Earth*, 123(10), 8957–8978. doi: 10.1029/2018JB016048
603 Huang, Z., Zhao, D., & Wang, L. (2015). P wave tomography and anisotropy beneath Southeast Asia:
604 Insight into mantle dynamics. *Journal of Geophysical Research: Solid Earth*, 120(7), 5154–5174.
605 doi: 10.1002/2015JB012098
606 Hung, S. H., Chen, W. P., & Chiao, L. Y. (2011). A data-adaptive, multiscale approach of finite-frequency,
607 traveltime tomography with special reference to P and S wave data from central Tibet. *Journal of*
608 *Geophysical Research: Solid Earth*, 116. doi: 10.1029/2010JB008190

Kind, R., Yuan, X., Saul, J., Nelson, D., Sobolev, S., Mechie, J., Zhao, W., Kosarev, G., Ni, J., Achauer, U., & Jiang, M. (2002). Seismic images of crust and upper mantle beneath Tibet: Evidence for Eurasian plate subduction. *Science*, 298(5596), 1219–1221. doi: 10.1126/science.1078115

Legendre, C. P., Deschamps, F., Zhao, L., & Chen, Q.-F. (2015). Rayleigh-wave dispersion reveals crust-mantle decoupling beneath eastern Tibet. *Scientific Reports*, 5(1), 1–7. doi: 10.1038/srep16644

Lei, J., Li, Y., Xie, F., Teng, J., Zhang, G., Sun, C., & Zha, X. (2014). Pn anisotropic tomography and dynamics under eastern Tibetan Plateau. *Journal of Geophysical Research: Solid Earth*, 119(3), 2174–2198. doi: 10.1002/2013JB010847

Lev, E., Long, M. D., & van der Hilst, R. D. (2006). Seismic anisotropy in Eastern Tibet from shear wave splitting reveals changes in lithospheric deformation. *Earth and Planetary Science Letters*, 251(3-4), 293-304. doi: 10.1016/j.epsl.2006.09.018

Li, H., Su, W., Wang, C.-Y., & Huang, Z. (2009). Ambient noise Rayleigh wave tomography in western Sichuan and eastern Tibet. *Earth and Planetary Science Letters*, 282(1-4), 201–211. doi: 10.1016/j.epsl.2009.03.021

Li, W., Chen, Y., Liang, X., & Xu, Y.-G. (2021). Lateral seismic anisotropy variations record interaction between Tibetan mantle flow and plume-strengthened Yangtze Craton. *Journal of Geophysical Research: Solid Earth*, 126, e2020JB020841. https://doi.org/10.1029/2020JB020841

Lin, F., Ritzwoller, M. H., Yang, Y., Moschetti, M. P., & Fouch, M. J. (2011). Complex and variable crustal and uppermost mantle seismic anisotropy in the western United States, *Nature Geoscience*, 4, 55–61.

Lin, Y., & Zhao, L. (2024). Upper-mantle anisotropy in the southeastern margin of Tibetan Plateau revealed by fullwave SKS splitting intensity tomography [Data set]. *Zenodo*. https://doi.org/10.5281/zenodo.10668695

Lin, Y.-P., Zhao, L., & Hung, S.-H. (2014a). Full-wave effects on shear wave splitting, *Geophysical Research Letters*, 41(3), 799–804. doi: 10.1002/2013GL058742

Lin, Y.-P., Zhao, L., & Hung, S.-H. (2014b). Full-wave multiscale anisotropy tomography in Southern California. *Geophysical Research Letters*, 41(24), 8809–8817. doi: 10.1002/ 2014GL061855

Link, F., Reiss, M. C., & Rümpker, G. (2022). An automatized XKS-splitting procedure for large data sets: Extension package for SplitRacer and application to the USArray. *Computers & Geosciences*, 158, 104961. doi: 10.1016/j.cageo.2021.104961

Liu, J., Wu, J., Wang, W., Fang, L., & Chang, K. (2020). Seismic anisotropy beneath the eastern margin

of the Tibetan Plateau from SKS splitting observations. *Tectonophysics*, 785, 228430. doi: 10.1016/j.tecto.2020.228430

Liu, Q. Y., van Der Hilst, R. D., Li, Y., Yao, H. J., Chen, J. H., Guo, B., Qi, S. H., Wang, J., Huang, H., & Li, S. C. (2014). Eastward expansion of the Tibetan Plateau by crustal flow and strain partitioning across faults. *Nature Geoscience*, 7(5), 361–365. doi: 10.1038/NGEO2130

Long, M. D., & Becker, T. W. (2010). Mantle dynamics and seismic anisotropy. *Earth and Planetary Science Letters*, 297(3-4), 341–354.

Mondal, P., & Long, M. D. (2019). A model space search approach to finite-frequency SKS splitting intensity tomography in a reduced parameter space. *Geophysical Journal International*, 217, 238-256. doi: 10.1093/gji/ggz016

Mondal, P., & Long, M. D. (2020). Strong seismic anisotropy in the deep upper mantle beneath the Cascadia backarc: Constraints from probabilistic finite-frequency SKS splitting intensity tomography. *Earth and Planetary Science Letters*, 539, 116172. doi: 10.1016/j.epsl.2020.116172

Montagner, J.-P., & Nataf, H.-C. (1986). A simple method for inverting the azimuthal anisotropy of surface waves, *Journal of Geophysical Research*, 91(B1), 511-520.

Monteiller, V., & Chevrot, S. (2011). High-resolution imaging of the deep anisotropic structure of the San Andreas Fault system beneath southern California. *Geophysical Journal International*, 186(2), 418-446. doi: 10.1111/j.1365-246X.2011.05082.x

Paige, C. C., & Saunders, M. A. (1982). LSQR–an algorithm for sparse linear-equations and sparse least-squares. *ACM Transactions on Mathematical Software*, 8(1), 43–71.

Pasyanos, M. E., Masters, T. G., Laske, G., & Ma, Z. (2014). LITHO1. 0: An updated crust and lithospheric model of the Earth. *Journal of Geophysical Research: Solid Earth*, 119(3), 2153–2173. doi: 10.1002/2013JB010626

Quatieri, T. F. (2006). *Discrete-time Speech Signal Processing: Principles and Practice*. Pearson Education India.

Royden, L. H., Burchfiel, B. C., & van der Hilst, R. D. (2008). The geological evolution of the Tibetan Plateau. *Science*, 321(5892), 1054–1058. doi: 10.1126/science.1155371

Shen, Z.-K., Lü, J., Wang, M., & Bürgmann, R. (2005). Contemporary crustal deformation around the southeast borderland of the Tibetan Plateau. *Journal of Geophysical Research: Solid Earth*, 110(B11). doi: 10.1029/2004JB003421

Shi, Y., Gao, Y., Su, Y., & Wang, Q. (2012). Shear-wave splitting beneath Yunnan area of Southwest

China. *Earthquake Science*, 25(1), 25–34. doi: 10.1007/s11589-012-0828-4

Sieminski, A., Paulssen, H., Trampert, J., & Tromp, J. (2008). Finite-frequency SKS splitting: measurement and sensitivity kernels. *Bulletin of the Seismological Society of America*, 98(4), 1797–1810. doi: 10.1785/0120070297

Sun, Y., Niu, F., Liu, H., Chen, Y., & Liu, J. (2012). Crustal structure and deformation of the SE Tibetan plateau revealed by receiver function data. *Earth and Planetary Science Letters*, 349, 186-197. doi: 10.1016/j.epsl.2012.07.007

Wang, C.-Y., Chan, W. W., & Mooney, W. D. (2003). Three-dimensional velocity structure of crust and upper mantle in southwestern China and its tectonic implications. *Journal of Geophysical Research: Solid Earth*, *108*(B9). doi: 10.1029/2002JB001973

Wang, C.-Y., Flesch, L. M., Silver, P. G., Chang, L.-J., & Chan, W. W. (2008). Evidence for mechanically coupled lithosphere in central Asia and resulting implications. *Geology*, 36(5), 363–366. doi: 10.1130/G24450A.1

Wang, C.-Y., Lou, H., Silver, P. G., Zhu, L., & Chang, L. (2010). Crustal structure variation along 30°N in the eastern Tibetan Plateau and its tectonic implications. *Earth and Planetary Science Letters*, 289(3-4), 367–376. doi: 10.1016/j.epsl.2009.11.026

Wang, M., & Shen, Z.-K. (2020). Present-day crustal deformation of continental China derived from GPS and its tectonic implications. *Journal of Geophysical Research: Solid Earth*, 125(2), e2019JB018774. doi: 10.1029/2019JB018774

Wang, W., Wu, J., Fang, L., Lai, G., & Cai, Y. (2017). Crustal thickness and Poisson's ratio in southwest China based on data from dense seismic arrays. *Journal of Geophysical Research: Solid Earth*, 122(9), 7219–7235. doi: 10.1002/2017JB013978

Wei, W., Xu, J., Zhao, D., & Shi, Y. (2012). East Asia mantle tomography: New insight into plate subduction and intraplate volcanism. *Journal of Asian Earth Sciences*, 60, 88–103. doi: 10.1016/j.jseaes.2012.08.001

Wei, Z., & Zhao, L. (2019). Lg-Q model and its implication on high-frequency ground motion for earthquakes in the Sichuan and Yunnan region. *Earth and Planetary Physics*, 3(6), 526–536. doi: 10.26464/epp2019054

Wei, Z., & Zhao, L. (2022). P-wave velocity structure of the lower crust and uppermost mantle beneath the Sichuan-Yunnan (China) region. *Seismological Research Letters*, 93(4). doi: 10.1785/0220210357

Wessel, P., Luis, J., Uieda, L., Scharroo, R., Wobbe, F., Smith, W. H., & Tian, D. (2019). The generic mapping tools version 6. *Geochemistry, Geophysics, Geosystems*, 20(11), 5556–5564. doi: 10.1029/2019GC008515

Xu, L., Rondenay, S., & van der Hilst, R. D. (2007). Structure of the crust beneath the southeastern Tibetan Plateau from teleseismic receiver functions. *Physics of the Earth and Planetary Interiors*, 165(3-4), 176–193. doi: 10.1016/j.pepi.2007.09.002

Xu, M., Huang, Z., Wang, L., Xu, M., Zhang, Y., Mi, N., Yu, D., & Yuan, X. (2020). Sharp lateral Moho variations across the SE Tibetan margin and their implications for plateau growth. *Journal of Geophysical Research: Solid Earth*, 125(5), e2019JB018117. doi: 10.1029/2019JB018117

Xu, Y., Chung, S.-L., Jahn, B.-m., & Wu, G. (2001). Petrologic and geochemical constraints on the petrogenesis of Permian–Triassic Emeishan flood basalts in southwestern China. *Lithos*, 58, 145–168.

Yang, S., Liang, X., Jiang, M., Chen, L., He, Y., Mon, C. T., Hou, G., Thant, M., Sein, K., & Wan, B. (2022). Slab remnants beneath the Myanmar terrane evidencing double subduction of the Neo-Tethyan Ocean. *Science Advances*, 8(34), eabo1027. doi: 10.1126/sciadv.abo1027

Yang, Y., Liang, C., Fang, L., Su, J., & Hua, Q. (2018). A comprehensive analysis on the stress field and seismic anisotropy in eastern Tibet. *Tectonics*, 37(6), 1648–1657. doi: 10.1029/2018TC005011

Yang, H., Peng, H., & Hu, J. (2017). The lithospheric structure beneath southeast Tibet revealed by P and S receiver functions. *Journal of Asian Earth Sciences*, 138, 62–71. https://doi.org/10.1016/j.jseaes.2017.02.001

Yang, Y., Yao, H., Wu, H., Zhang, P., & Wang, M. (2019). A new crustal shear-velocity model in Southwest China from joint seismological inversion and its implications for regional crustal dynamics. *Geophysical Journal International*, 220, 1379–1393. https://doi.org/10.1093/gji/ggz514

Yang, Y., Zheng, Y., Chen, J., Zhou, S., Celyan, S., Sandvol, E., Tilmann, F., Priestley, K., Hearn, T. M., Ni, J. F., Brown, L. D., & Ritzwoller, M. H. (2010). Rayleigh wave phase velocity maps of Tibet and the surrounding regions from ambient seismic noise tomography. *Geochemistry, Geophysics, Geosystems*, 11(8). doi:10.1029/2010GC003119

Yao, H. J., van der Hilst, R. D., & Montagner, J. P. (2010). Heterogeneity and anisotropy of the lithosphere of SE Tibet from surface wave array tomography. *Journal of Geophysical Research: Solid Earth*, 115. doi: 10.1029/2009JB007142

Yin, A., & Harrison, T. M. (2000). Geologic evolution of the Himalayan-Tibetan orogen. *Annual Review*

of Earth and Planetary Sciences, 28(1), 211–280.

Zhang, F., Wu, Q., Li, Y., Zhang, R., Sun, L., Pan, J., & Ding, Z. (2018). Seismic tomography of eastern Tibet: Implications for the Tibetan Plateau growth. *Tectonics*, 37(9), 2833–2847. doi: 10.1029/2018TC004977

Zhang, G. W., Guo, A. L., Wang, Y. J., Li, S. Z., Dong, Y. P., Liu, S. F., He, D. F., Cheng, S. Y., Lu, R. K., & Yao, A. P. (2013). Tectonics of South China Continent and its implications. *Science China Earth Sciences*, 56, 1804–1828. doi: 10.1007/s11430-013-4679-1

Zhang, P., Deng, Q., Zhang, G., Ma, J., Gan, W., Min, W., Mao, F., & Wang, Q. (2003). Active tectonic blocks and strong earthquakes in the continent of China. *Science China Earth Sciences*, 46(2), 13–24. doi: 10.1360/03dz0002

Zhang, P.-Z. (2013). A review on active tectonics and deep crustal processes of the western Sichuan region, eastern margin of the Tibetan Plateau. *Tectonophysics*, 584, 7–22. doi: 10.1016/j.tecto.2012.02.021

Zhang, Z., Wang, Y., Chen, Y., Houseman, G. A., Tian, X., Wang, E., & Teng, J. (2009). Crustal structure across Longmenshan fault belt from passive source seismic profiling. *Geophysical Research Letters*, 36(17). doi: 10.1029/2009GL039580

Zhang, Z., Yao, H., & Yang, Y. (2020). Shear wave velocity structure of the crust and upper mantle in Southeastern Tibet and its geodynamic implications. *Science China Earth Sciences*, 63, 1278–1293. https://doi.org/10.1007/s11430-020-9625-3

Zhang, Z., Feng, J., & Yao, H. (2023). 3-D azimuthal anisotropy structure reveals different deformation modes of the crust and upper mantle in the southeastern Tibetan Plateau. *Frontiers in Earth Science*, 11, 1095609. doi: 10.3389/feart.2023.1095609

Zhao, G., Unsworth, M. J., Zhan, Y., Wang, L., Chen, X., Jones, A. G., Tang, J., Xiao, Q., Wang, J., Cai, J., Li, T., Wang, Y., & Zhang, J. (2012). Crustal structure and rheology of the Longmenshan and Wenchuan Mw 7.9 earthquake epicentral area from magnetotelluric data. *Geology*, 40(12), 1139–1142. doi: 10.1130/ G33703.1

Zhao, L., & Chevrot, S. (2011). An efficient and flexible approach to the calculation of three-dimensional full-wave fréchet kernels for seismic tomography—II. Numerical results. *Geophysical Journal International*, 185(2), 939–954. doi: 10.1111/j.1365-246X.2011.04984.x

Zhao, L., Jordan, T. H., & Chapman, C. H. (2000). Three-dimensional Fréchet differential kernels for seismic delay times**,** *Geophysical Journal International*, 141(3), 558–576. doi: 10.1046/j.1365-

246x.2000.00085.x

Zhao, L. F., Xie, X. B., He, J. K., Tian, X., & Yao, Z. X. (2013). Crustal flow pattern beneath the Tibetan Plateau constrained by regional Lg-wave Q tomography. *Earth and Planetary Science Letters*, 383, 113–122. doi: 10.1016/j.epsl.2013.09.038.

Figure Captions

Figure 1. Map of the tectonic environment of SE margin of Tibetan Plateau with seismic stations (green-filled triangles) and epicenters (red open circles) of earthquakes of magnitude 5 and above from 2000 to 2022. The blue triangle marks the station WXT for which SKS waveforms, splitting intensities and sensitivity kernels are shown in Figures 4, 5 and 7, respectively. Major active faults are shown by thick black lines with abbreviated names in black, including LMSF: Longmenshan Fault; XSHF: Xianshuihe Fault; JSJF: Jinshajiang Fault; LCJF: Lancangjiang Fault; LJ-XJHF: Lijiang-Xiaojinhe Fault; ANH-ZMHF: Anninghe-Zemuhe Fault; XJF: Xiaojiang Fault; and RRF: Red River Fault. Major active tectonic blocks are indicated by abbreviated texts in blue, including SGT: Songpan-Ganzi Terrane; SCB: Sichuan Basin; QTB: Qiangtang Block; SYRB: Sichuan-Yunnan Rhombic Block; YTC: Yangtze Craton; and ICB: Indo-China Block. EHS stands for the Eastern Himalaya Syntax. Blue cross arrows show the surface strain rate derived from GPS observation (Wang & Shen, 2020). Background color shows the topography. The black box in the inset map indicates the location of the main figure.

Figure 2. Lithosphere thickness map. The global model LITHO1.0 (Pasyanos et al., 2014) is shown for the region north of 27ºN, whereas to the south the regional model of Yang et al. (2017) is depicted. Names of major faults and tectonic blocks are the same as in Figure 1.

Figure 3. Distribution of 470 teleseismic events used for SKS splitting intensity inversion in this study. Events of magnitudes Mw5.5 and greater in the epicentral distance range of 90°–130° during 2009–2020 are selected. The red box in the center indicates the study area.

Figure 4. An example of SKS window selection using SplitRacer. (a) and (b) show normalized radial and transverse records, respectively, around the SKS arrival at station WXT (blue triangle in Figure 1) from the 24 June 2019 earthquake in New Zealand with a back azimuth of 122º. The green lines mark the theoretical SKS and SKKS arrival times corresponding to the event of interest. Red vertical lines mark the start and end times of the final window used for SI measurement. (c) Summed spectral power of the spectrogram of the radial and transverse records in (a) and (b). The red horizontal line marks the frequency of maximum spectral power, and the red dashed lines show the frequency bounds of more than 80% of the maximum. The green vertical lines mark the time window in which the summed spectral power is more than 50% of the maximum. (d) Summed spectral power over all frequencies. The green vertical lines mark the time window in which the summed spectral energy is more than 50% of the maximum. (e) STA/LTA ratio of the radial-component record used as quality check. The blue vertical line denotes the time when the STA/LTA ratio reaches its peak within the window determined in (d). The red horizontal

line is the acceptance threshold of 2.1 (Link et al., 2022).

Figure 5. Variations of measured SI with event back azimuth for station WXT (blue triangle in Figure 1) before (a) and after (b) removal of SI outliers. The vertical error bars show two standard deviations ($2\sigma_i$) of individual measurements. The dashed lines represent the sinusoidal curves that best fit the measurements. According to Eq. (2), the conventional SKS splitting parameters for this station are: $\Delta t = 1.08$ s and $\theta = 109.14°$.

Figure 6. Black line segments show the conventional SKS fast-direction azimuths and delay times at all station obtained from the SI measurements according to Eq. (2). Red line segments are fast-direction azimuths and delay times derived from Eq. (2) based on the model-predicted SIs obtained by integrating the sensitivity kernels (see Figure 7) with the anisotropy model in Figure 12 according to Eq. (4). Names of major faults and tectonic blocks are the same as in Figure 1.

Figure 7. Examples of the sensitivity kernels of the SI to shear wave anisotropy parameters γ_c (a) and γ_s (b) shown in mapviews for the 146-km depth and in profiles (insets) along source-receiver path AA' for station WXT (blue triangle in Figure 1). The SKS wave is from the 24 June 2019 event in New Zealand with a back azimuth of 122º, and the waveforms are shown in Figure 4.

Figure 8. Resolution tests for the azimuth of symmetry axis using 1º x 1º checkerboard. (Top-left) The input model has horizontally alternating azimuthal angles of fast axes $\phi_f = 90^\circ$ and $\phi_f = 45^\circ$ shown by both the color and the directions of the line segments, and a fixed anisotropy strength $\gamma = 4\%$ represented by the lengths of the line segments. The two white dashed lines show the locations of profiles NS and N'S' in Figure 11. The other panels show the recovered models at a depth of 55 km for different damping factors λ. We choose $\lambda = 4$ as the optimal value for the damping factor (top-right panel). Red triangles show locations of stations used.

Figure 9. Resolution test using 1º x 1º checkerboard. (Top-left) The input model has horizontally alternating anisotropy strengths shown by the colors representing perturbations of $\delta\gamma = \pm 3\%$ relative to a background anisotropy strength of $\gamma = 4\%$, and a fixed azimuthal angle of symmetry axis $\phi_f = 22.5^\circ$. The other panels show the recovered models at a depth of 55 km for different damping factors λ. We choose $\lambda = 4$ as the optimal value for the damping factor (top-right panel).

Figure 10. Resolution test using 1º x 1º checkerboard with damping factor $\lambda = 4$. (Upper panels) Recovered model at the depths of 99 km, 165 km, 208 km and 274 km for an input model having horizontally alternating azimuthal angles of fast axes $\phi_f = 90^\circ$ and $\phi_f = 45^\circ$ with a fixed anisotropy strength $\gamma = 4\%$. The input model and the recovered model at 55-km depth are shown in Figure 8. (Lower

panels) Recovered model at the depths of 99 km, 165 km, 208 km and 274 km for an input model with horizontally alternating anisotropy strengths of $\gamma = 1\%$ and $\gamma = 7\%$ (perturbations of $\delta\gamma = \pm 3\%$ relative to a background anisotropy strength of $\gamma = 4\%$) with a fixed azimuthal angle of symmetry axis $\phi_f = 22.5^{\circ}$. The input model and the recovered model at 55-km depth are shown in Figure 9.

Figure 11. Resolution tests for an input model with 4 layers of alternating azimuthal angles of symmetry axes $\phi_f = 45^{\circ}$ and $\phi_f = 135^{\circ}$ but a fixed anisotropy strength of $\gamma = 4\%$. Shown here are the input model (top-left panel) and recovered models for different damping factors λ along the north-south cross-section NS through the middle of the study region (see top-left panel in Figure 8). The optimal damping is $\lambda = 4$ (middle-left panel).

Figure 12. Three-dimensional anisotropic model for the SE margin of Tibetan Plateau at 55 km, 99 km, 165 km, 208 km and 274 km depths. The anisotropy strength and the azimuth of the fast axes are shown by the background color and the black line segments, respectively. The lengths of the line segments are proportional to the anisotropy strength. The black and green arrows denote the absolute plate motion (APM) of the Eurasian and Indian plates, respectively, according to the model NNR-MORVEL56 (Argus et al., 2011). The white dashed lines show locations of the profiles shown in Figure 13. Names of major faults and tectonic blocks are the same as in Figure 1. Blue triangles show locations of stations used. Regions in which the recovery errors are above 20% are mask out. The recovery error is defined by $E = \left(\left|\phi_f - \tilde{\phi}_f\right|/90^{\circ}\right) \times 100\%$, where $\tilde{\phi}_f$ and ϕ_f are the input and recovered azimuthal angles in the resolution tests in Figures 8 and 10.

Figure 13. Vertical profiles of the azimuths of fast axis in our 3D anisotropy model along (a) 26ºN latitude, (b) 32ºN latitude, (c) 100ºE longitude and (d) 104ºE longitude. The azimuths of the fast axis are shown by the background color. Note that red (~0º) and blue (~180º) colors both indicate nearly N-S fast axis, whereas yellow color indicates nearly E-W fast axis. Moho and lithosphere-asthenosphere boundary (LAB) are depicted by thick black and white lines, respectively. Names of major faults and tectonic blocks are the same as in Figure 1.

Figure 14. Result of the recovery test. The recovered and input anisotropic models are compared at five depths marked at the bottom-right corner in each panel. Black and red line segments denote the directions of fast axes in the input and recovered models, respectively, and their lengths indicates the anisotropy strength. Names of major faults and tectonic blocks are the same as in Figure 1. Blue triangles show locations of stations used.

Figure 15. Comparison of SKS splitting times and fast axis directions predicted by our anisotropy model

(Figure 12) with previous studies. Black line segments are results from the present study, whereas blue and red line segments show results from Chang et al. (2015) and Liu et al. (2020), respectively. Blue and red ellipses highlight stations where there are large discrepancies in splitting parameters between this study and Liu et al. (2020) and Chang et al. (2015), respectively. Names of major faults and tectonic blocks are the same as in Figure 1.

Manuscript submitted to Journal of Geophysical Research: Solid Earth

Supporting Information for

Upper-mantle anisotropy in the southeastern margin of Tibetan Plateau revealed by fullwave SKS splitting intensity tomography

Yi Lin[1,2] and Li Zhao[1,3*]

[1] *School of Earth and Space Sciences, Peking University, Beijing 100871, China.*
[2] *Key Laboratory of Earth Exploration and Information Techniques of the China Ministry of Education, Chengdu University of Technology, Chengdu 610059, China.*
[3] *Hebei Hongshan National Geophysical Observatory, Peking University, Beijing 100871, China.*

* Corresponding author: Li Zhao (lizhaopku@pku.edu.cn)

This Supporting Information contains 14 Supplementary Figures S1-S14.

Figure S1: Resolution test results at different depths for 45º variation in the azimuth of symmetry axis using 1º x 1º checkerboard and different damping factors.
Figure S2: Resolution test results at different depths for 45º variation in the azimuth of symmetry axis using 1.5º x 1.5º checkerboard and different damping factors.
Figure S3: Resolution test results at different depths for 90º variation in the azimuth of symmetry axis using 1º x 1º checkerboard and different damping factors.
Figure S4: Resolution test results at different depths for 90º variation in the azimuth of symmetry axis using 1.5º x 1.5º checkerboard and different damping factors.
Figure S5: Resolution test results at different depths for anisotropy strength using 1º x 1º checkerboard and different damping factors.
Figure S6: Resolution test results at different depths for anisotropy strength using 1.5º x 1.5º checkerboard and different damping factors.
Figure S7: Resolution tests for the azimuth of symmetry axis using a 2-layer input model and different damping factors.
Figure S8: Resolution tests for anisotropy strength using a 2-layer input model and different damping factors.
Figure S9: Resolution tests for the azimuth of symmetry axis using a 4-layer input model and different damping factors.
Figure S10: Resolution tests for anisotropy strength using a 4-layer input model and different damping factors.

Figure S11. Resolution tests result at 55-km depth for the azimuth of symmetry axis using 1º x 1º checkerboard with a substantially increased standard deviation (0.3 s) of the Gaussian noise.

Figure S12. Result at different depth for the same resolution test as Figure S11.

Figure S13. Resolution tests result at 55-km depth for anisotropy strength using 1º x 1º checkerboard with a substantially increased standard deviation (0.3 s) of the Gaussian noise.

Figure S14. Result at different depth for the same resolution test as Figure S13.

Supplementary Figures

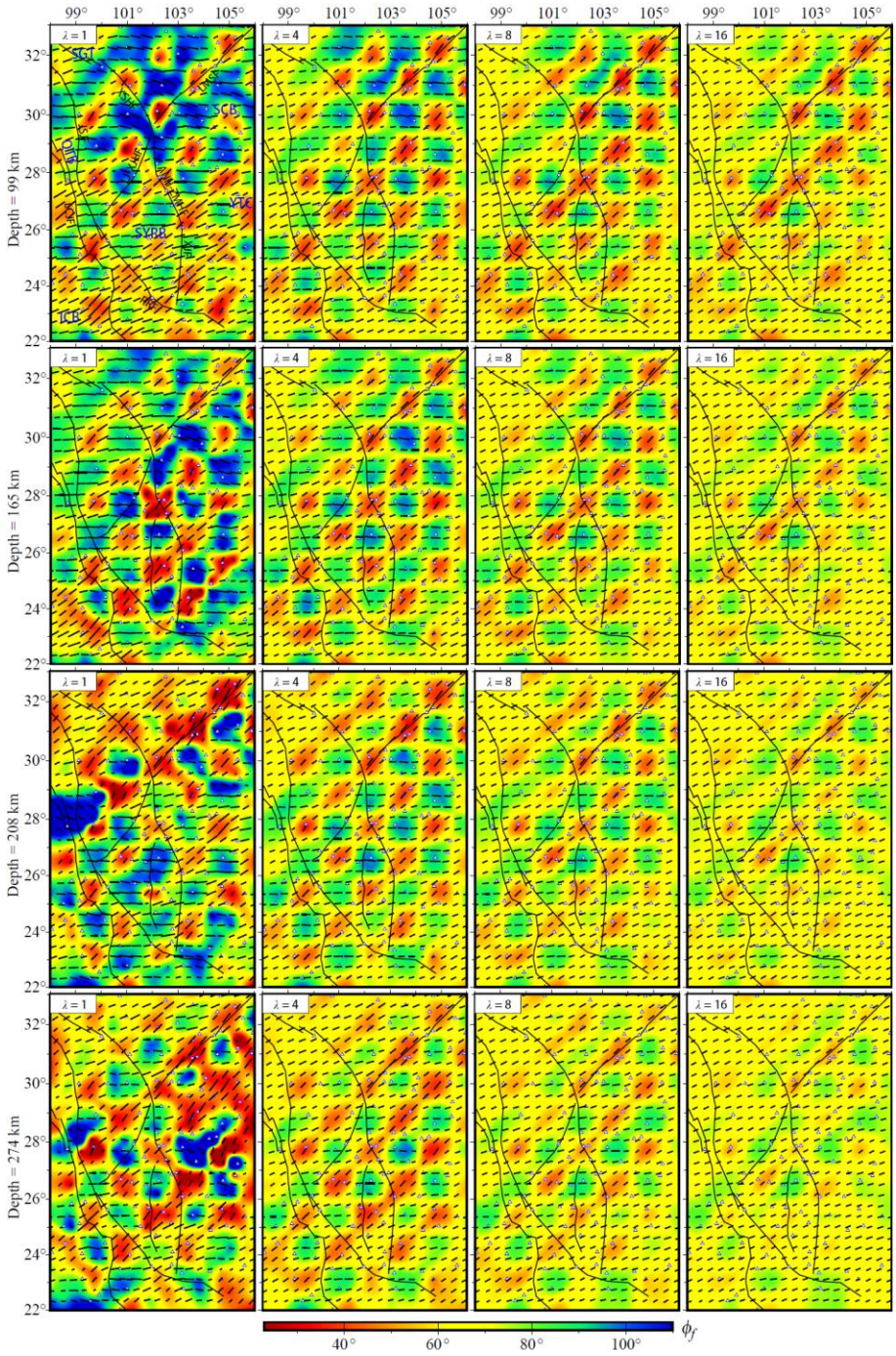

Figure S1. Resolution tests for the azimuth of symmetry axis using 1º x 1º checkerboard. The input model (top-left panel of Figure 8) has horizontally alternating azimuthal angles of fast axes $\phi_f = 90^\circ$ and $\phi_f = 45^\circ$ shown by both the color and the directions of the line segments, and a fixed anisotropy strength $\gamma = 4\%$ represented by the lengths of the line segments. Shown here are recovered models using different damping factors (left to right) at different depths (top to bottom).

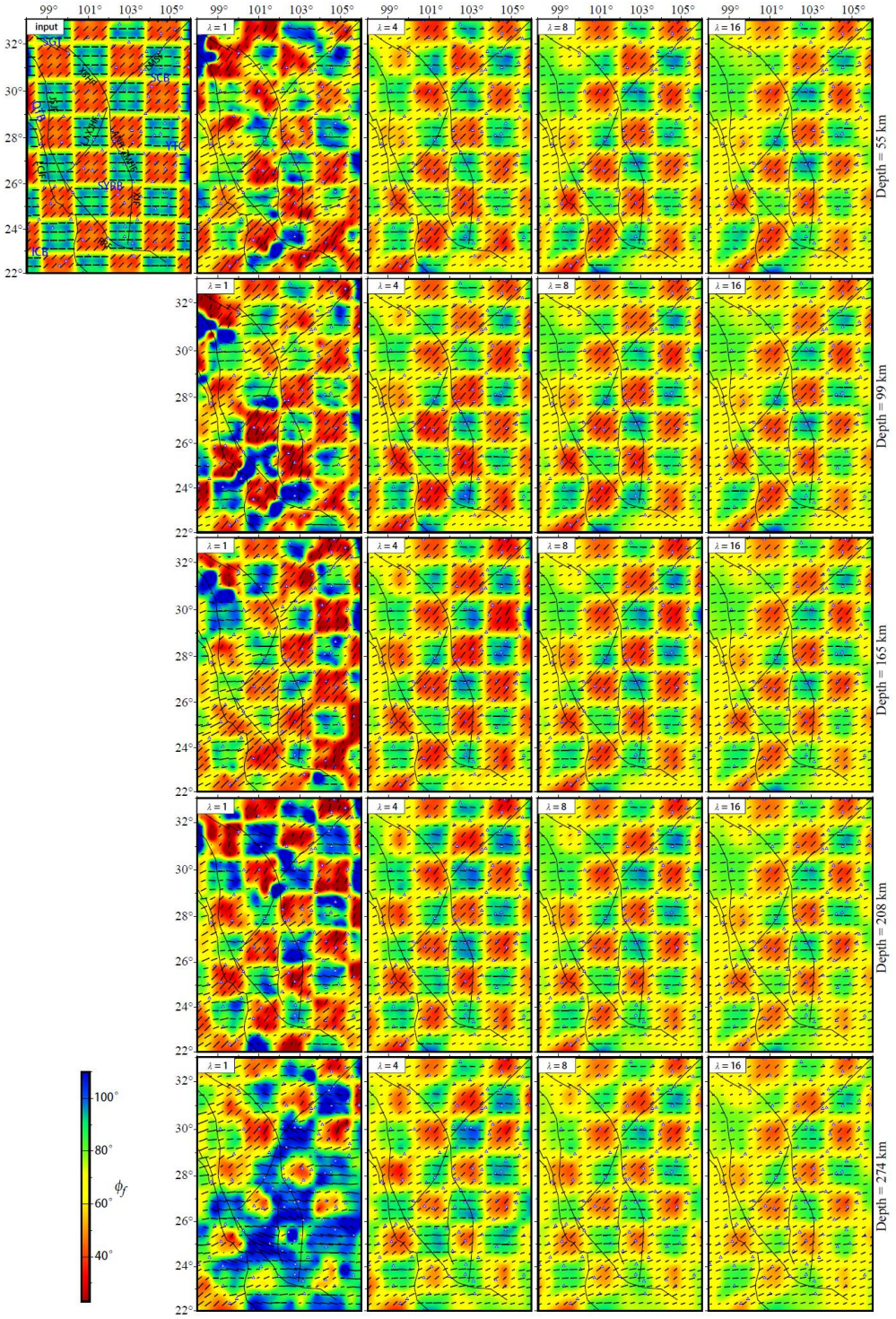

Figure S2. Resolution tests for the azimuth of symmetry axis using 1.5º x 1.5º checkerboard. The input model (top-left panel) has horizontally alternating azimuthal angles of fast axes $\phi_f = 90^\circ$ and $\phi_f = 45^\circ$ shown by both the color and the directions of the line segments, and a fixed anisotropy strength $\gamma = 4\%$ represented by the lengths of the line segments. The rest of the panels show recovered models using different damping factors (left to right) at different depths (top to bottom).

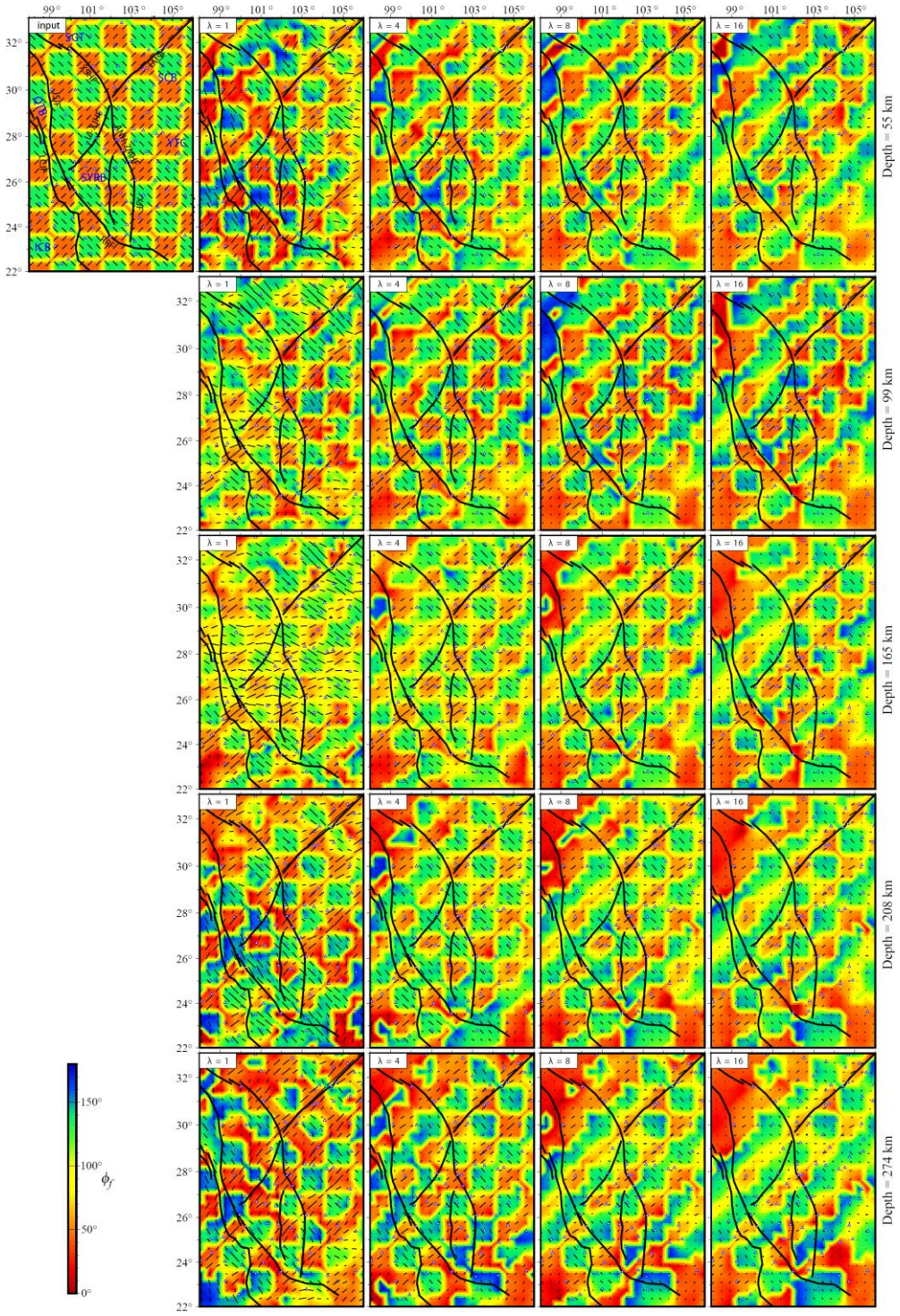

Figure S3. Resolution tests for the azimuth of symmetry axis using 1º x 1º checkerboard. The input model (top-left panel) has horizontally alternating azimuthal angles of fast axes $\phi_f = 45^\circ$ and $\phi_f = 135^\circ$ shown by both the color and the directions of the line segments, and a fixed anisotropy strength $\gamma = 4\%$ represented by the lengths of the line segments. Shown here are recovered models using different damping factors (left to right) at different depths (top to bottom).

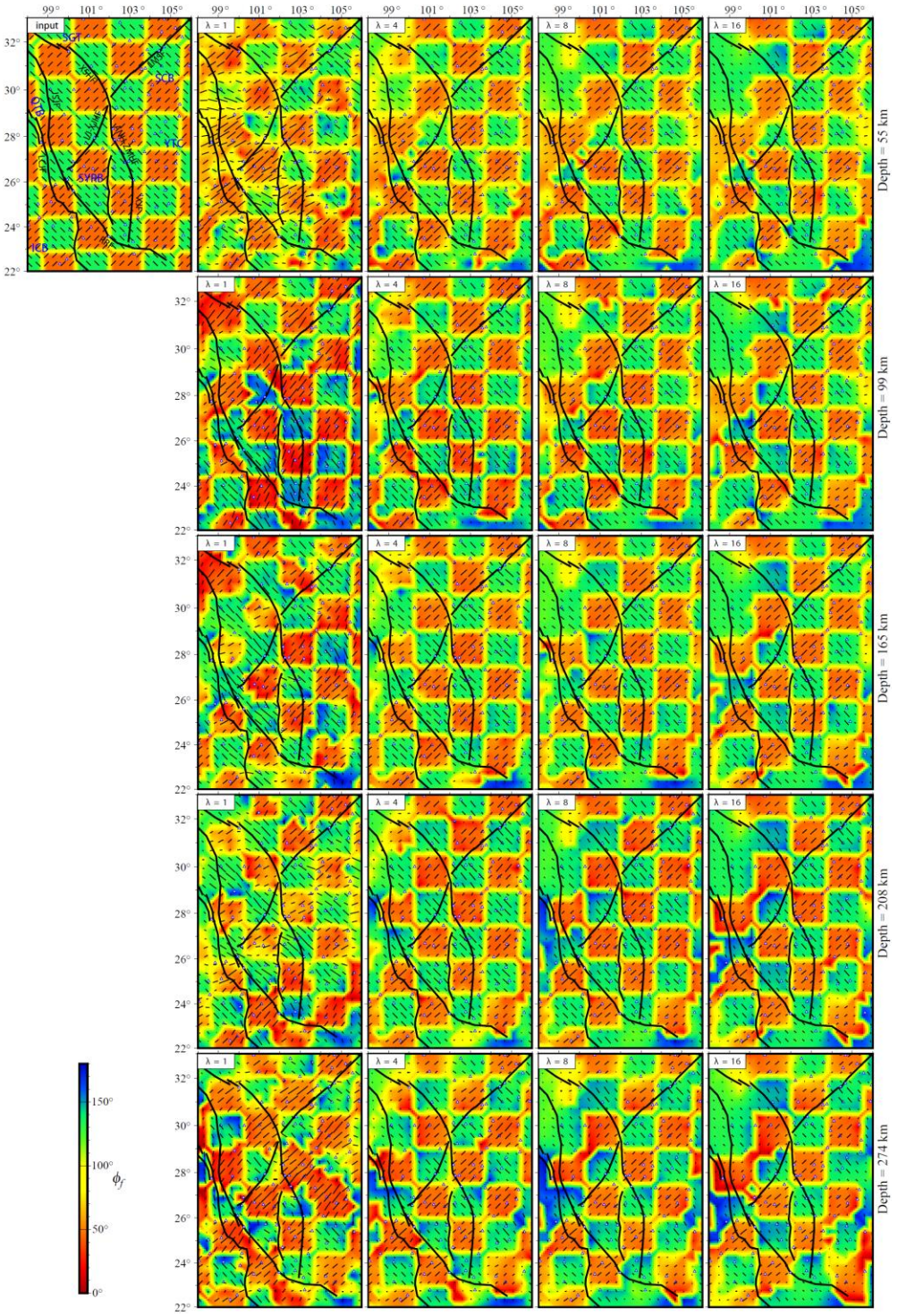

Figure S4. Resolution tests for the azimuth of symmetry axis using 1.5º x 1.5º checkerboard. The input model (top-left panel) has horizontally alternating azimuthal angles of fast axes $\phi_f = 45^\circ$ and $\phi_f = 135^\circ$ shown by both the color and the directions of the line segments, and a fixed anisotropy strength $\gamma = 4\%$ represented by the lengths of the line segments. The rest of the panels show recovered models using different damping factors (left to right) at different depths (top to bottom).

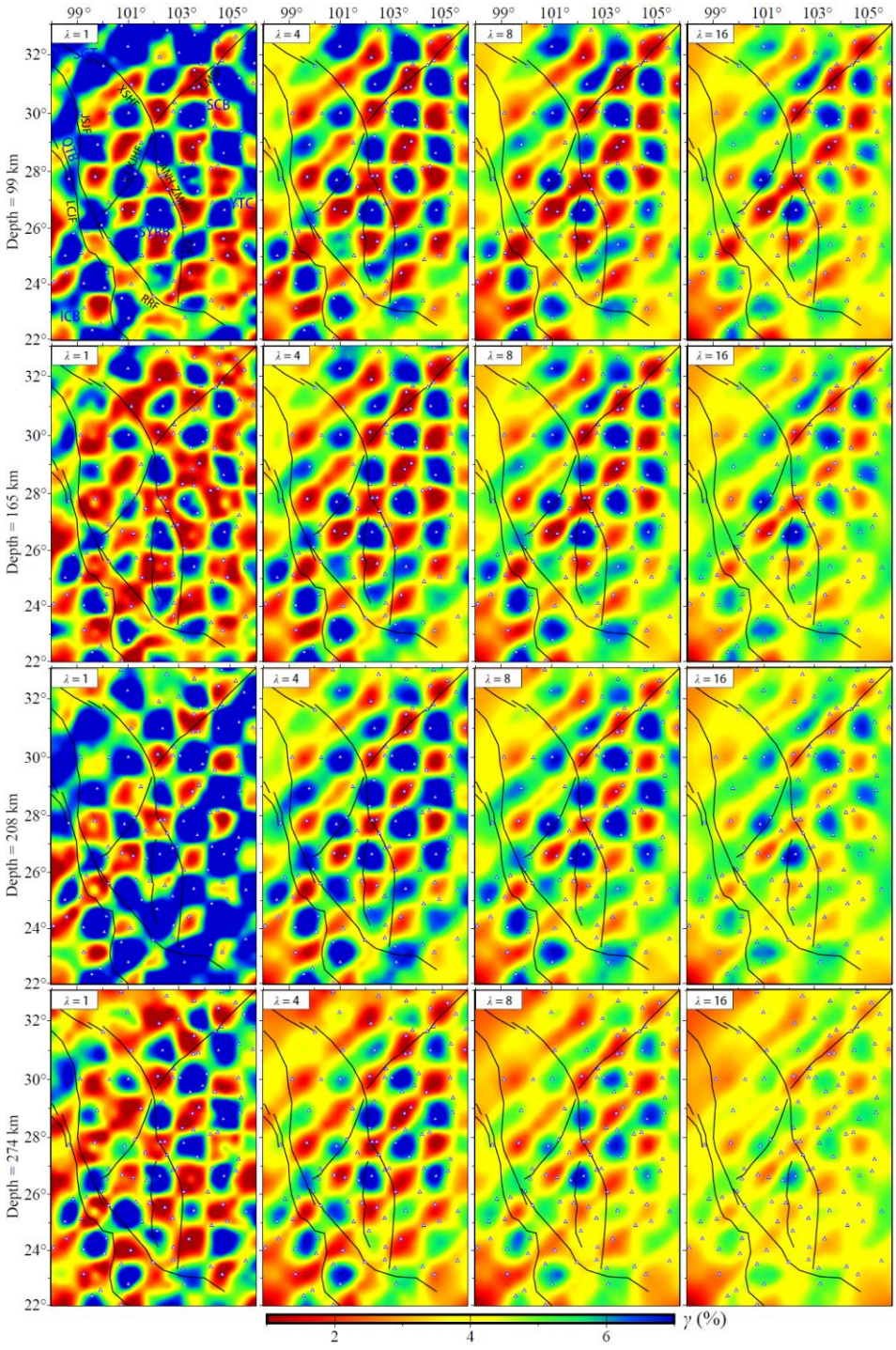

Figure S5. Resolution tests for anisotropy strength using 1º x 1º checkerboard. The input model (top-left panel of Figure 8) has horizontally alternating anisotropy strengths shown by the colors representing perturbations of $\delta\gamma = \pm 0.03$ relative to a background anisotropy strength of $\gamma = 0.04$ and a fixed azimuthal angle of symmetry axis $\phi_f = 22.5^{\circ}$. Shown here are recovered models using different damping factors (left to right) at different depths (top to bottom).

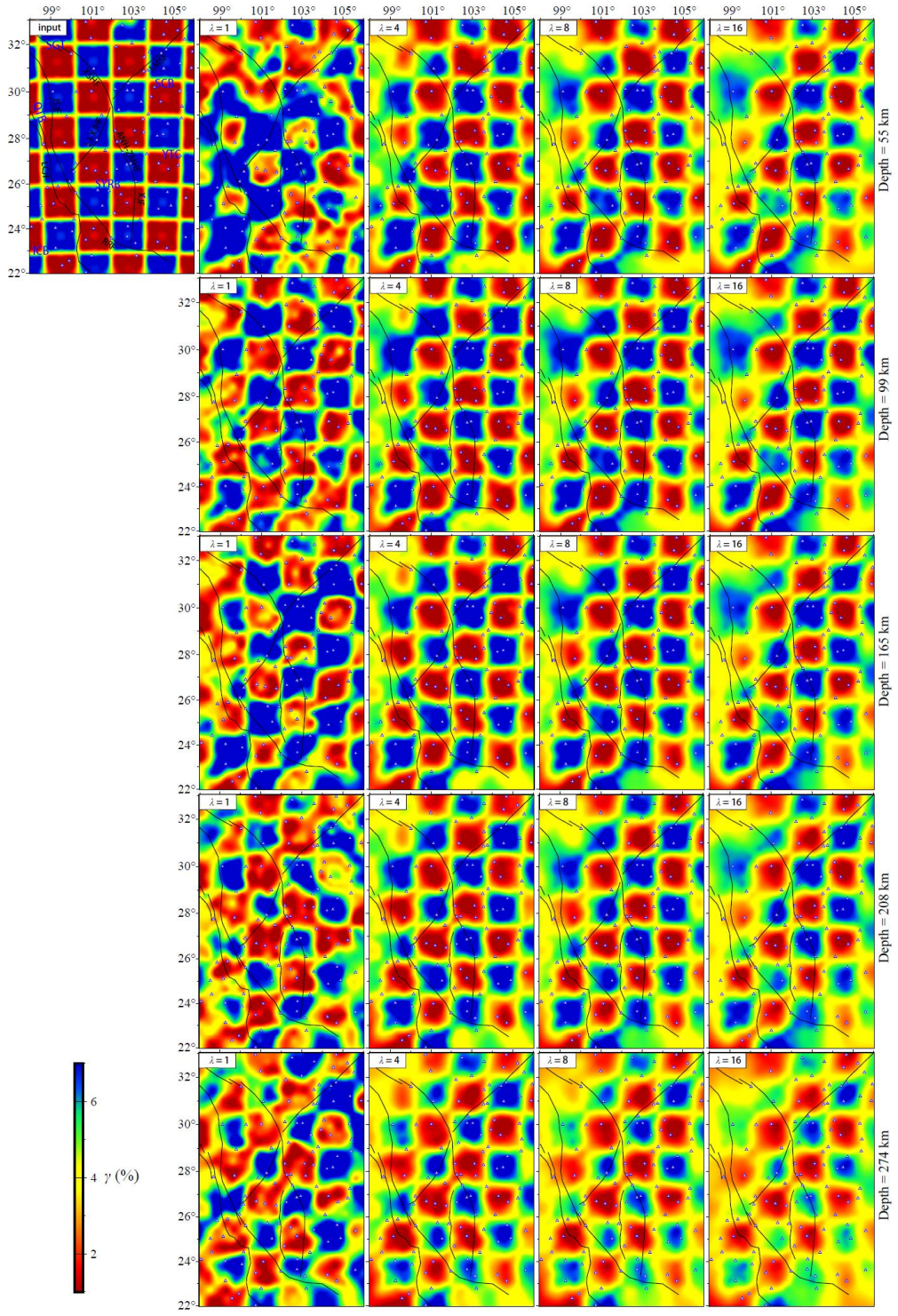

Figure S6. Resolution tests for anisotropy strength using 1.5º x 1.5º checkerboard. The input model (top-left panel) has horizontally alternating anisotropy strengths shown by the colors representing perturbations of $\delta\gamma = \pm 0.03$ relative to a background anisotropy strength of $\gamma = 0.04$ and a fixed azimuthal angle of symmetry axis $\phi_f = 22.5^{\circ}$. The rest of the panels show recovered models using different damping factors (left to right) at different depths (top to bottom).

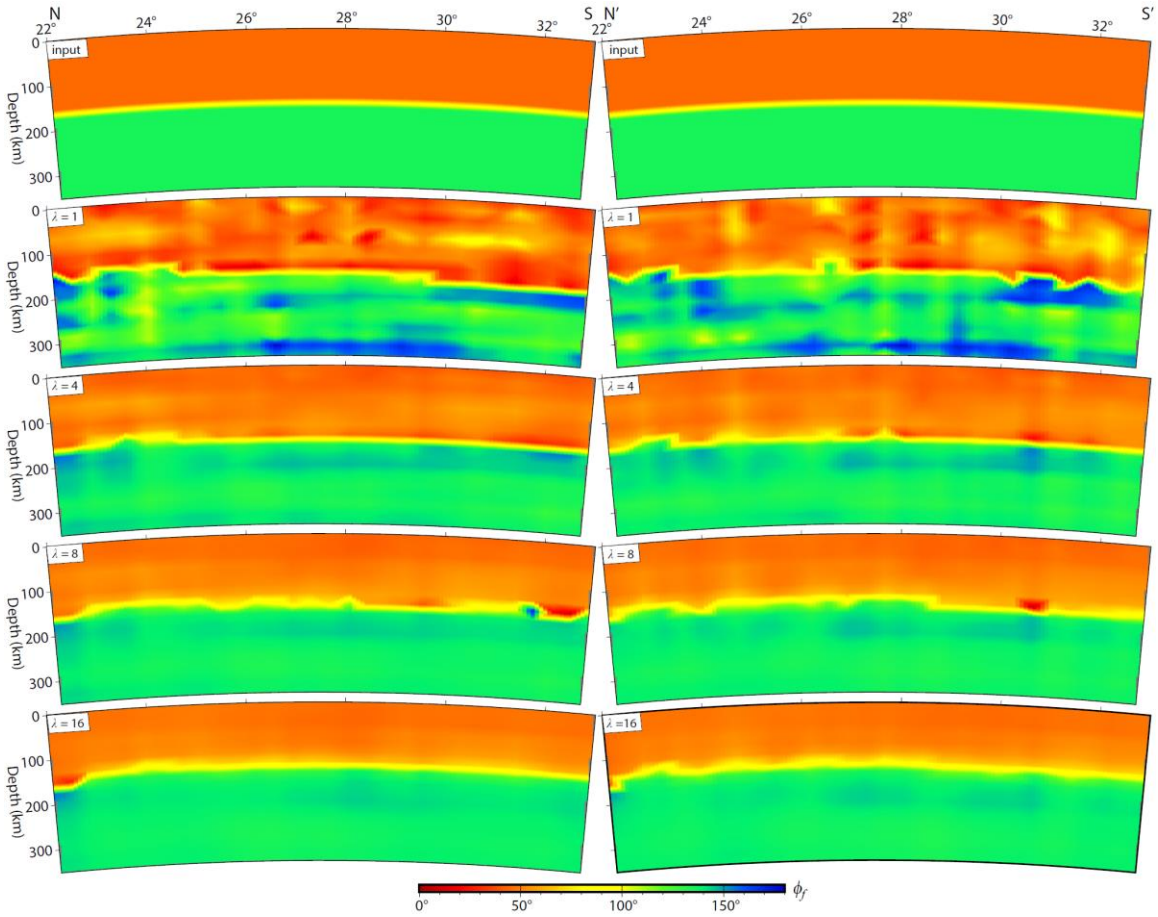

Figure S7. Resolution tests for an input model with 2 layers of different azimuthal angles of symmetry axes $\phi_f = 45^\circ$ and $\phi_f = 135^\circ$ but a fixed anisotropy strength of $\gamma = 4\%$. Shown here are the input models (top two panels) along the NS and N'S' cross-sections (see top-left panel in Figure 8 for the locations of the cross-sections) and recovered models for different damping factors λ (lower panels).

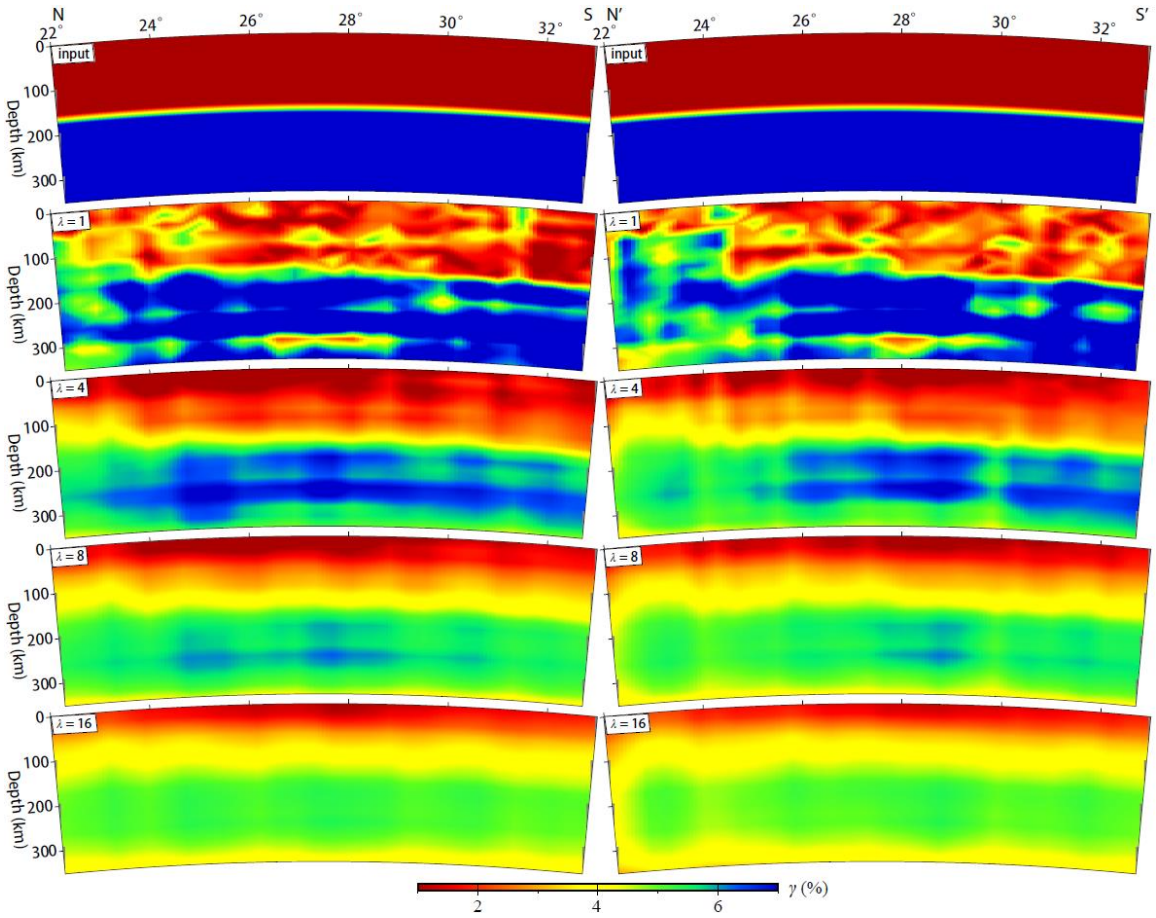

Figure S8. Resolution tests for an input model with 2 layers of different anisotropy strengths shown by the colors representing perturbations of $\delta\gamma = \pm 0.03$ relative to a background anisotropy strength of $\gamma = 0.04$ and a fixed azimuthal angle of symmetry axis $\phi_f = 22.5^{\circ}$. Shown here are the input models (top two panels) along the NS and N'S' cross-sections (see top-left panel in Figure 8 for the locations of the cross-sections) and recovered models for different damping factors λ (lower panels).

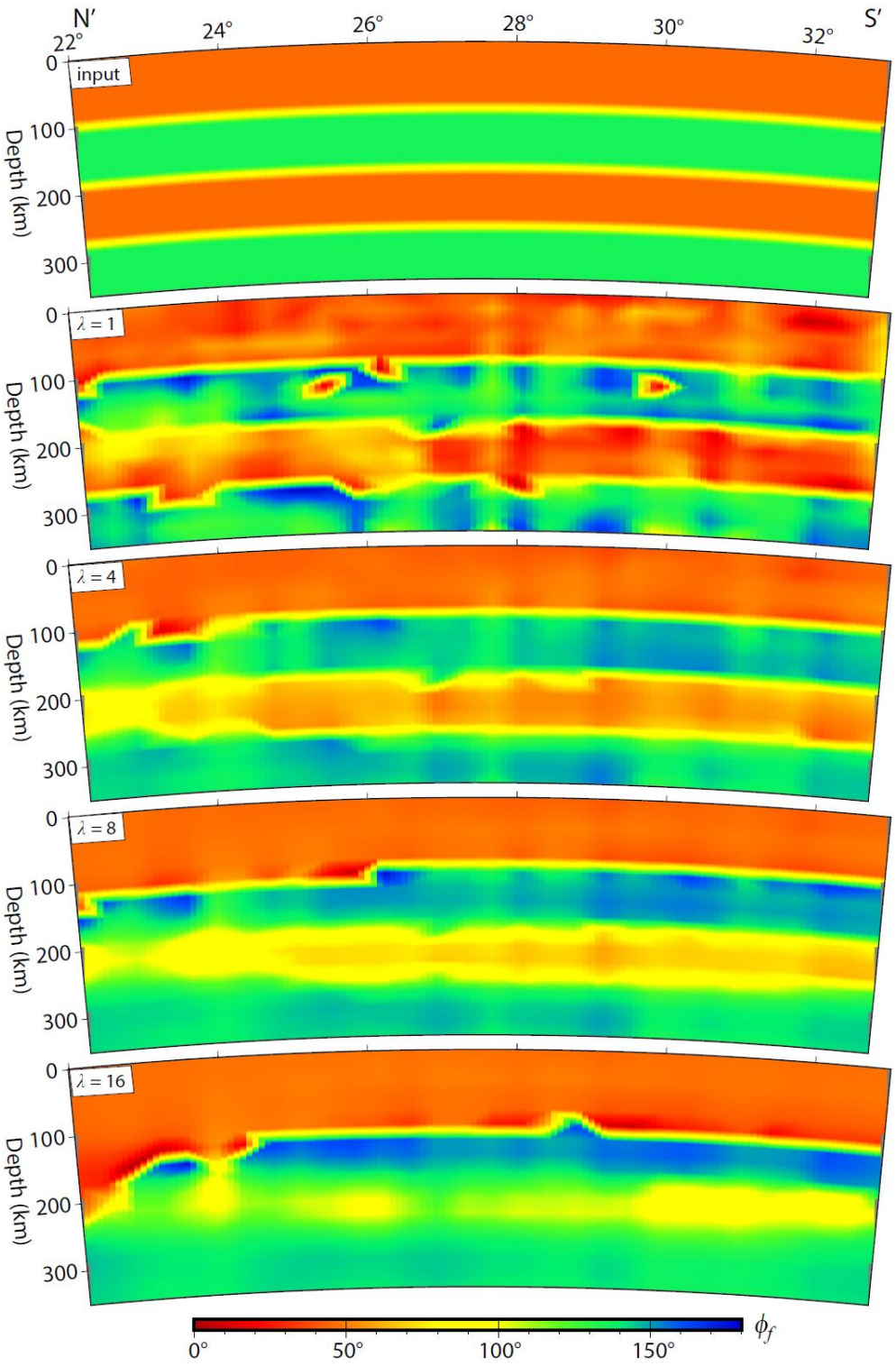

Figure S9. Resolution tests for an input model with 4 layers of alternating azimuthal angles of symmetry axes $\phi_f = 45^\circ$ and $\phi_f = 135^\circ$ but a fixed anisotropy strength of $\gamma = 4\%$. Shown here are the input model (top panel) along the N'S' cross-section (see top-left panel in Figure 8 for the location of the cross-section) and recovered models for different damping factors λ (lower panels).

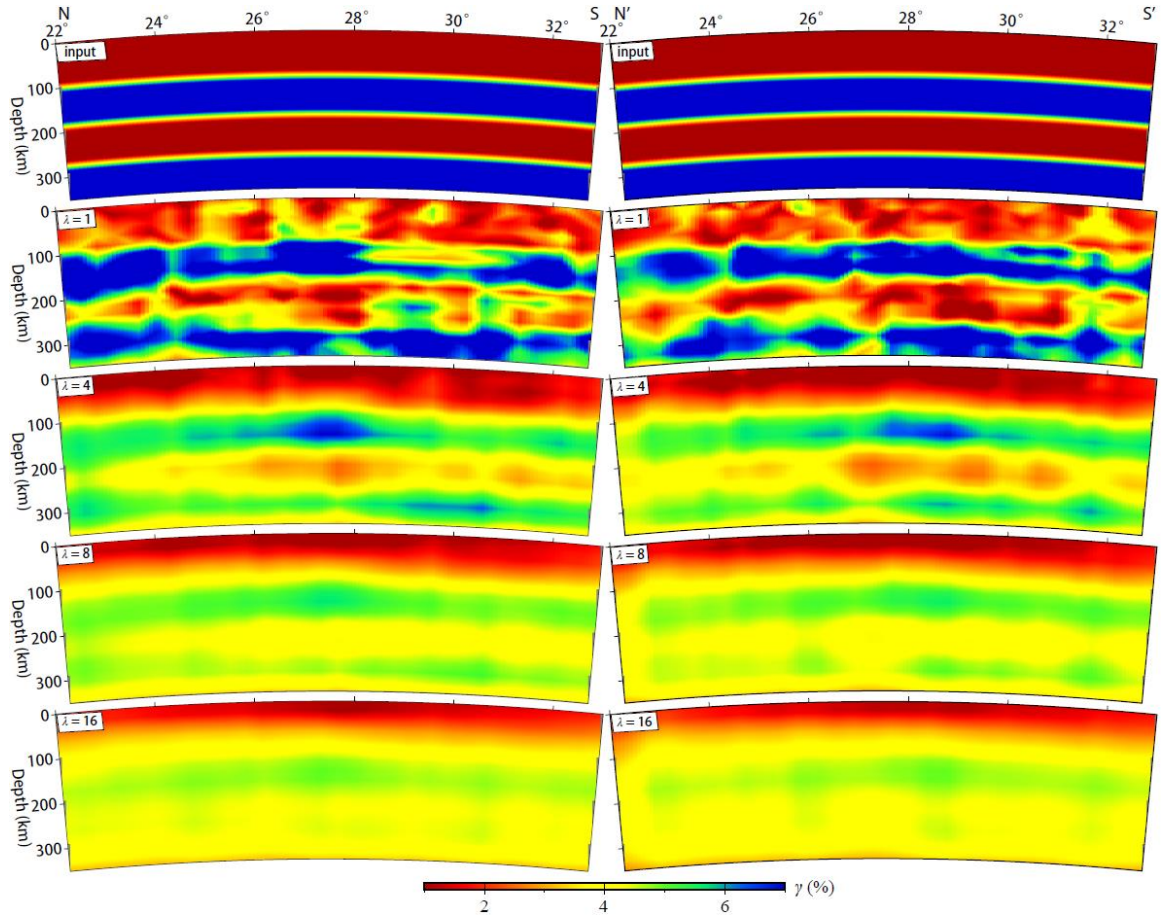

Figure S10. Resolution tests for an input model with 4 layers of alternating anisotropy strengths shown by the colors representing perturbations of $\delta\gamma = \pm 0.03$ relative to a background anisotropy strength of $\gamma = 0.04$ and a fixed azimuthal angle of symmetry axis $\phi_f = 22.5^{\circ}$. Shown here are the input models (top two panels) along the NS and N'S' cross-sections (see top-left panel in Figure 8 for the locations of the cross-sections) and recovered models for different damping factors λ (lower panels).

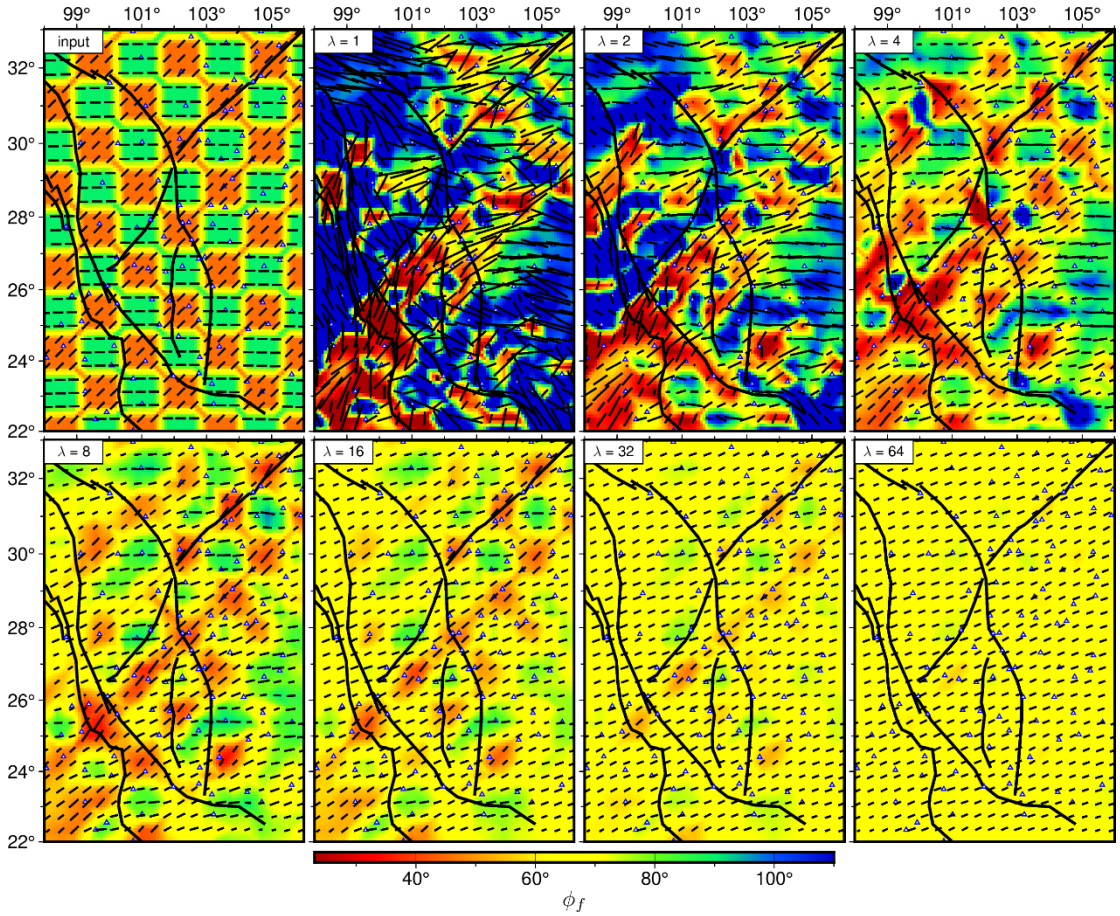

Figure S11. Resolution tests for the azimuth of symmetry axis using 1º x 1º checkerboard with substantially increased standard deviation (0.3 s) of the Gaussian noise. (Top-left) The input model has horizontally alternating azimuthal angles of fast axes $\phi_f = 90^\circ$ and $\phi_f = 45^\circ$ shown by both the color and the directions of the line segments, and a fixed anisotropy strength $\gamma = 4\%$ represented by the lengths of the line segments. The other panels show the recovered models at a depth of 55 km for different damping factors λ.

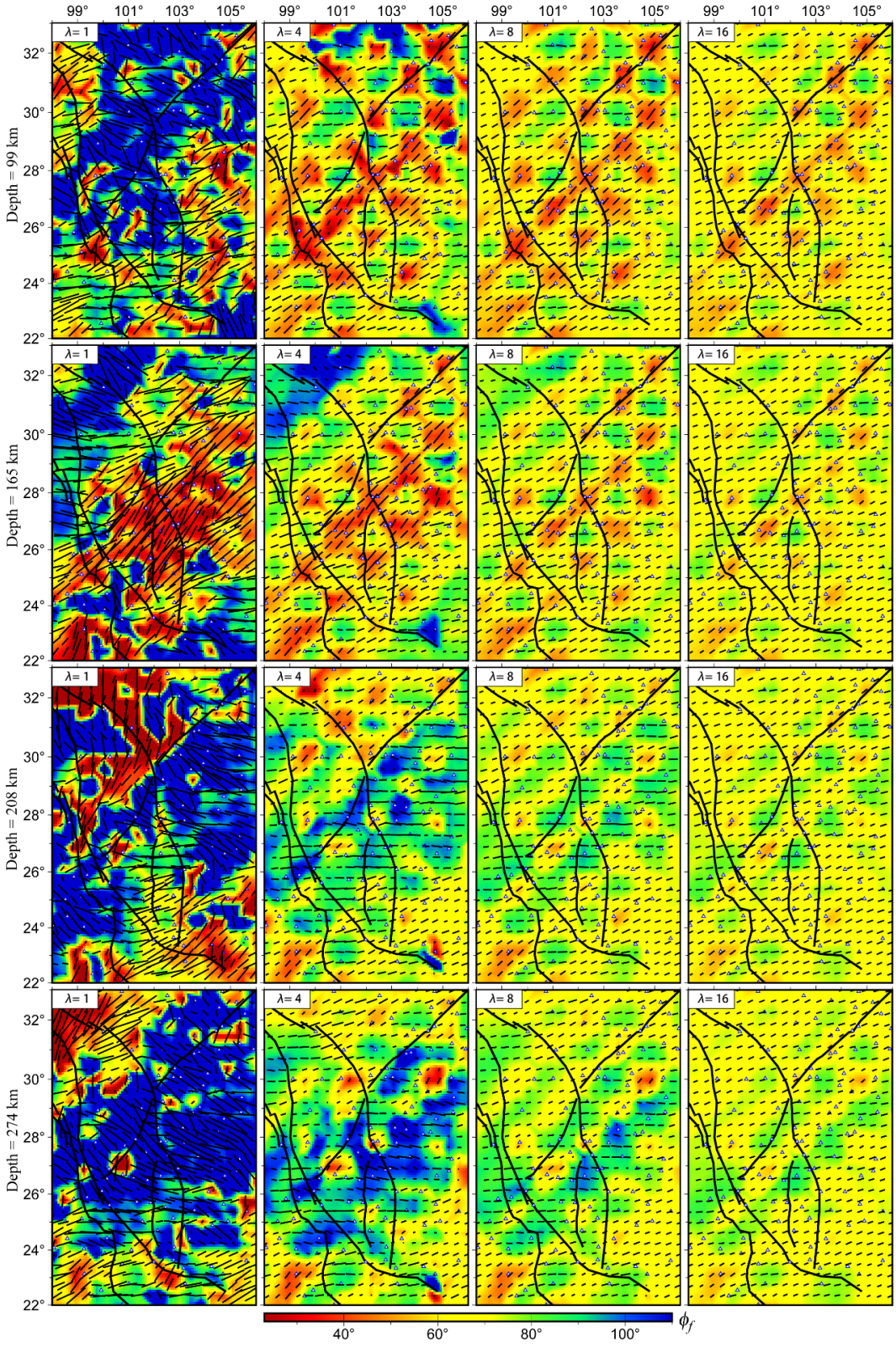

Figure S12. Recovered models for the same resolution test in Figure S11 using for different damping factors (left to right) at different depths (top to bottom).

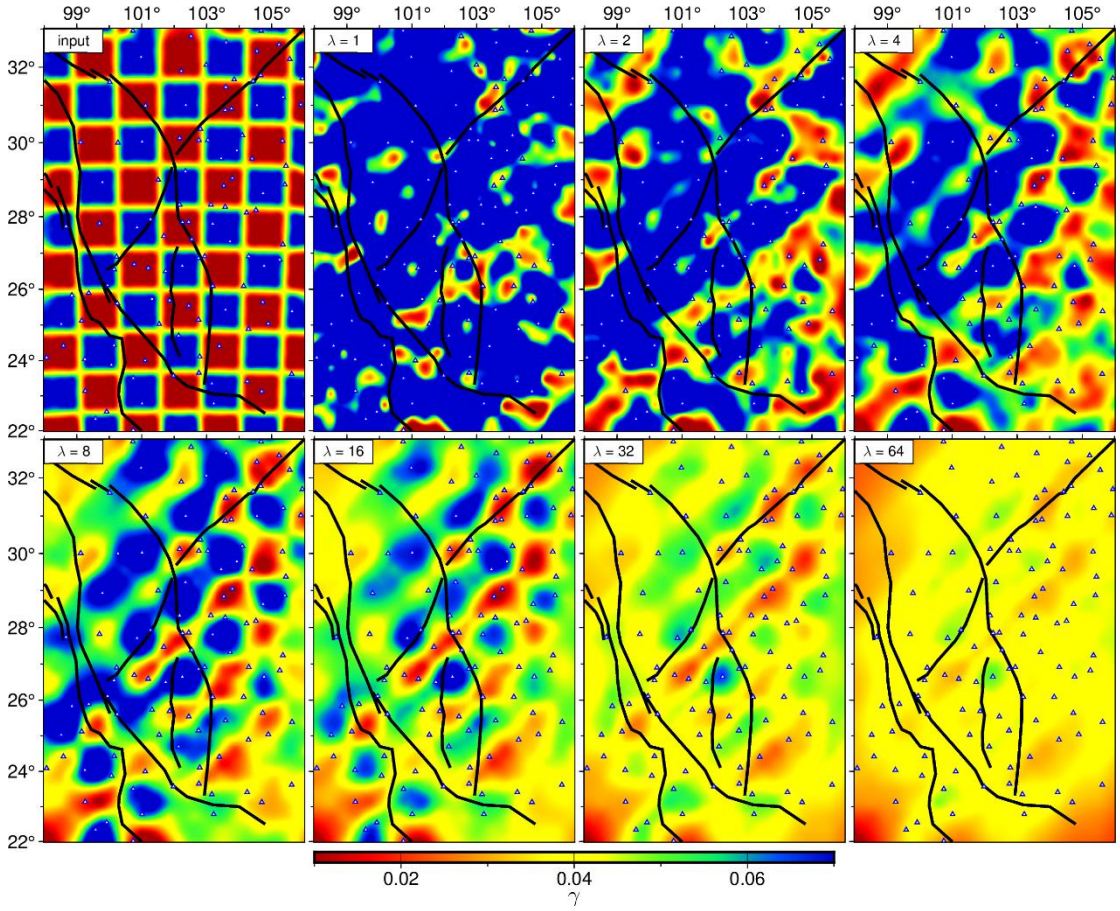

Figure S13. Resolution test for anisotropy strength using 1º x 1º checkerboard with substantially increased standard deviation (0.3 s) of the Gaussian noise. (Top-left) The input model has horizontally alternating anisotropy strengths shown by the colors representing perturbations of $\delta\gamma = \pm 3\%$ relative to a background anisotropy strength of $\gamma = 4\%$, and a fixed azimuthal angle of symmetry axis $\phi_f = 22.5^{\circ}$. The other panels show the recovered models at a depth of 55 km for different damping factors λ.

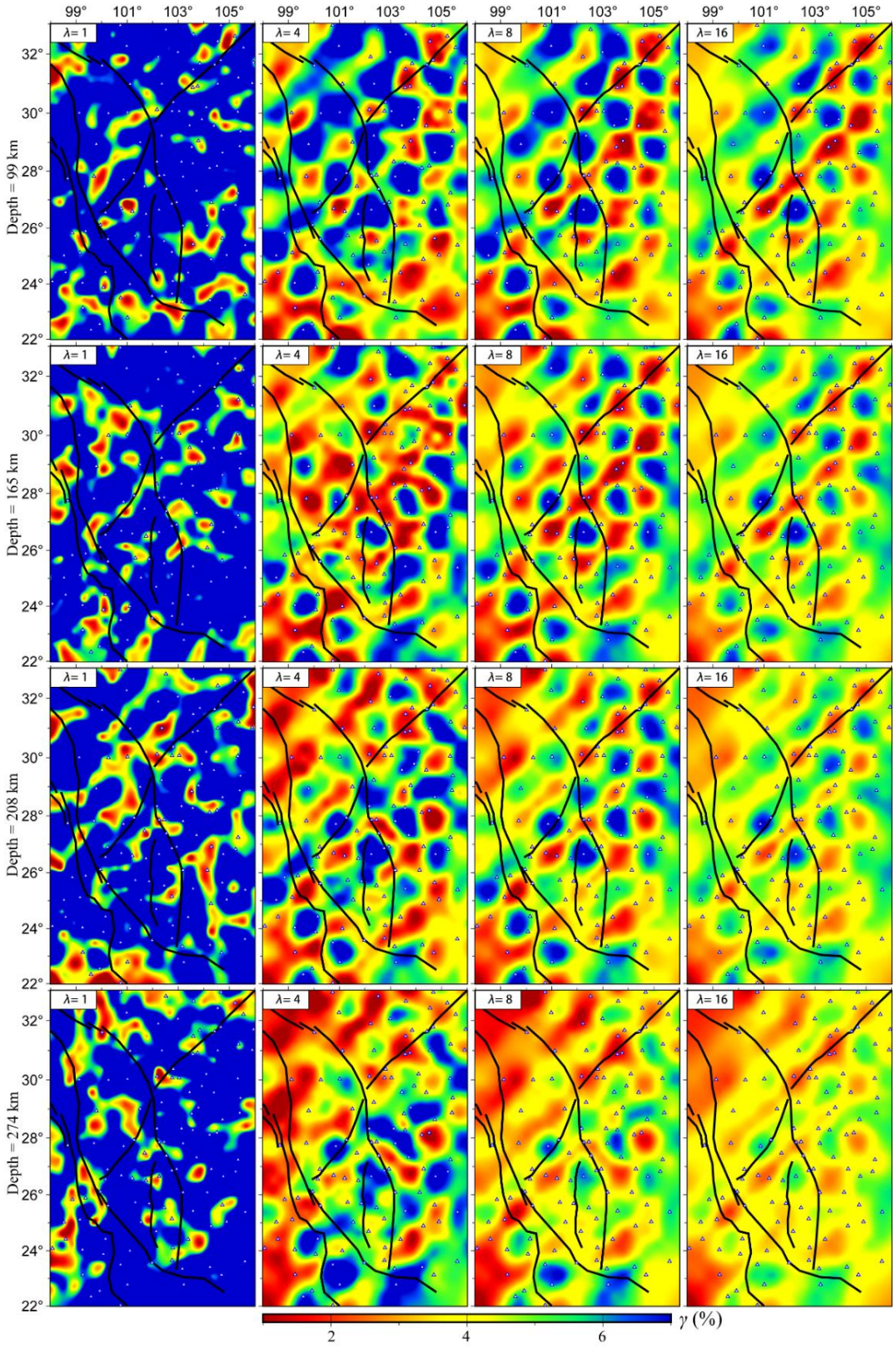

131

132 **Figure S14**. Recovered models for the same resolution test in Figure S13 using for different
133 damping factors (left to right) at different depths (top to bottom).